iScience

CellPress

Article

Discovery of a Vertebrate-Specific Factor that Processes Flagellar Glycolytic Enolase during Motile Ciliogenesis

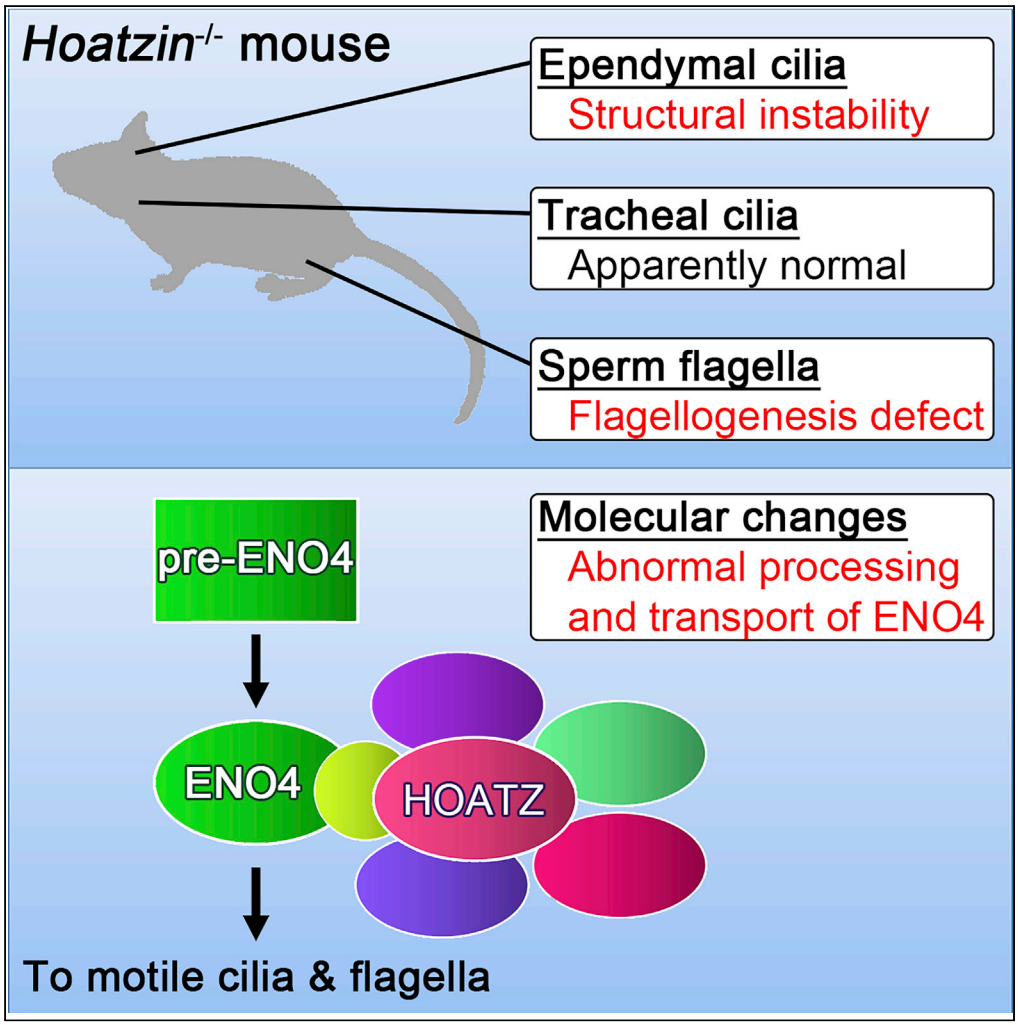

Keishi Narita, Hiroaki Nagatomo, Hiroko Kozuka-Hata, Masaaki Oyama, Sen Takeda

knarita@yamanashi.ac.jp (K.N.)
stakeda@yamanashi.ac.jp (S.T.)

HIGHLIGHTS

Knockout of *Hoatz* causes hydrocephalus and oligo-astheno-terato-zoospermia

Motile cilia are variably affected by the *Hoatz* mutation depending on tissue type

Candidate HOATZ-interacting proteins including ENO4 are identified

Knockout of *Hoatz* alters the western blot profile of ENO4

Narita et al., iScience *23*, 100992
April 24, 2020 © 2020 The Author(s).
https://doi.org/10.1016/j.isci.2020.100992

iScience

CellPress

Article

Discovery of a Vertebrate-Specific Factor that Processes Flagellar Glycolytic Enolase during Motile Ciliogenesis

Keishi Narita,[1,4,*] Hiroaki Nagatomo,[2] Hiroko Kozuka-Hata,[3] Masaaki Oyama,[3] and Sen Takeda[1,*]

SUMMARY

Motile cilia and flagella require ATP for their formation and function. Although glycolytic enzymes are components of flagellar proteomes, how they translocate to flagella is unknown. Here we show that the expression pattern of the functionally nonannotated gene *4833427G06Rik* (*C11orf88*), which is found only in vertebrates and is designated here as Hoatzin (*Hoatz*), suggests a functional association of its product with motile cilia and flagella. *Hoatz* knockout (KO) mice developed hydrocephalus and male infertility in an autosomal recessive manner, and the ependymal cilia frequently showed disorganized axonemes, reducing motility associated with collapsed spermatid flagella during cytodifferentiation. HOATZ was associated with certain proteins, including the flagellar glycolytic enzyme ENO4. In the testes of the *Hoatz* KO mice, the immature form of ENO4 accumulated in abnormal cytoplasmic puncta of developing spermatids. These data indicate that HOATZ is required for motile ciliogenesis and flagellar genesis in vertebrates by mediating the maturation of ENO4.

INTRODUCTION

Motile cilia and flagella are subcellular organelles of eukaryotes that propel extracellular fluids. A small number of vertebrate cell types express these structures under the regulation of specific transcription factors (Choksi et al., 2014; Gerdes et al., 2009) that are required for clearing airways, transport of gametes, circulating cerebrospinal fluid, or determining left-right asymmetry (Hirokawa et al., 2006; Zariwala et al., 2006). The typical internal architectures of the 9 + 2 axoneme (Lin et al., 2015); biogenesis, including the cytoplasmic preassembly of dynein arms (Olcese et al., 2017; Omran et al., 2008); and subsequent intraflagellar transport (Snell et al., 2004) are well conserved among eukaryotic species. ATP is required for their formation and motility through ATP-driven motor proteins such as kinesins and dyneins (Khan and Scholey, 2018). The flagellar proteome of *Chlamydomonas reinhardtii* comprises glycolytic enzymes, indicating the importance of *in situ* ATP production for flagellar motility (Mitchell, 2005; Pazour et al., 2005). Such glycolytic enzymes are involved in the second half of the glycolysis pathway (pay-off phase) in which the high-energy glucose metabolite glyceraldehyde 3-phosphate is converted into low-energy products (e.g., pyruvate) to produce ATP (Berg et al., 2011). However, insufficient data are available to show that these metabolic enzymes are actively transported into motile subcellular organelles or if their molecular mechanisms are conserved among eukaryotes.

Here we characterized a mouse gene of unknown function designated *4833427G06Rik* (*C11orf88*), which is identified in a group of 99 putative cilia-related genes in mammals (McClintock et al., 2007). Our unpublished analysis of *4833427G06Rik* revealed that its sequence is conserved only in vertebrates. We designate this gene here as Hoatzin [*Hoatz*] according to the hydrocephalus and oligo-astheno-terato-zoospermia phenotype of *Hoatz* KO mice. We therefore hypothesized that its product (HOATZ) contributes to a vertebrate-specific function associated with motile cilia and flagella. Moreover, our present data suggest that HOATZ mediates motile ciliogenesis by processing ENO4, a glycolytic enzyme expressed specifically in ciliated cells of vertebrates.

RESULTS

Hoatzin mRNA Is Specifically Expressed in Tissues with Motile Cilia and Flagella

During our search for novel cilia-related genes in mice, we identified a functionally nonannotated gene designated *4833427G06Rik*, which we named Hoatzin (*Hoatz*) according to the knockout (KO) phenotype

[1]Department of Anatomy and Cell Biology, Faculty of Medicine, University of Yamanashi, Chuo, Yamanashi 409-3898, Japan

[2]Center for Life Science Research, University of Yamanashi, Chuo, Yamanashi 409-3898, Japan

[3]Medical Proteomics Laboratory, Institute of Medical Science, The University of Tokyo, 4-6-1 Shirokanedai, Minato-ku, Tokyo 108-8639, Japan

[4]Lead Contact

*Correspondence: knarita@yamanashi.ac.jp (K.N.), stakeda@yamanashi.ac.jp (S.T.)

https://doi.org/10.1016/j.isci.2020.100992

This is an open access article under the CC BY license (http://creativecommons.org/licenses/by/4.0/).

described above and encodes a 19 kDa (147 amino acid residues) protein without a known functional domain. Significant amino acid sequence similarities were detected only among vertebrate proteins, including a highly conserved region near the C terminus (Figure 1A). Reverse-transcriptase polymerase chain reaction (RT-PCR) analysis of adult mouse tissues and primary cultured ependyma strongly suggest that gene expression was limited to the cells with motile cilia or flagella (Figure 1B). Furthermore, *Hoatz* mRNA was detected in cultured brain ependyma, lung, testis, and oviduct but not in whole brain, liver, kidney, spleen, and eyeball (Figure 1B and data not shown). *Hoatz* expression in testes was detected as early as postnatal day 15 (P15), which then continually increased during the first 45 days (Figure 1C). The first wave of spermatogenesis occurs during this time when primitive spermatogonia in the testes synchronously differentiate, and new populations of germ cells consecutively appear as follows: spermatocytes, P15; spermatids, P21; and spermatozoa, P42 (Zimmermann et al., 2015). RNA *in situ* hybridization analysis of a 4-week-old mouse testis detected *Hoatz* expression predominantly in haploid spermatids undergoing flagellogenesis at the luminal side of the seminiferous tubules (Figure 1D).

The subcellular localization of HOATZ was investigated using cultured ependyma expressing recombinant HOATZ-FLAG (Figure S1A). Immunostaining of the transduced cells detected the majority of the protein in the cytoplasm, although it was occasionally detected in the cilia (Figure S1B). When a small hairpin RNA (shRNA) targeting *Hoatz* mRNA was expressed in cultured ependyma, one (TRCN0000201969) of five clones exhibited abnormal ciliogenesis (data not shown). These observations suggest the importance of HOATZ for the motile cilia. Moreover, lentiviral transduction of *Hoatz* cDNA into the ependyma of a *Hoatz*$^{-/-}$ mouse rescued the phenotype of low ciliary beating frequency (Figure S1C). Immunostaining of the transduced *Hoatz*$^{-/-}$ ependyma using an anti-FLAG antibody detected the tagged HOATZ in the cilia (Figure S1D).

Knockout of Hoatz Causes Hydrocephalus and Oligo-Astheno-Terato-Zoospermia

We mutated *Hoatz* using CRISPR/Cas9 technology (Figure S2A) as described in detail in the Methods section. Among the six founder mutants screened using tail genome sequencing, only one transmitted mutations to the progeny. However, this female founder had chimeric mutations in germline cells and produced three strains, each with different indels (Figures S2B and S2C). Strain #1 had a single deletion of guanine at the double-strand break site, c31, resulting in a frameshift. Strain #2 had the same deletion but with insertion of CTA, again causing a frameshift. Strain #3 had a 114-nucleotide deletion around the target sequence and a 381-nucleotide insertion downstream of the target sequence. Strain #3 was mainly used because of the simplicity of its genotyping (Figure S2D). HOATZ expression in strain #3 was undetectable using a HOATZ-specific rabbit polyclonal antibody (Figures S2E–S2G).

Hoatz$^{-/-}$ mice exhibited hydrocephalus and oligo-astheno-terato-zoospermia (Figure 2), which was inherited in an autosomal recessive manner and observed in the progeny of six generations of backcrosses with a C57BL/6N background. Varying severities of hydrocephalus were observed in the *Hoatz*$^{-/-}$ mutants (Figures 2A and 2B). Some mice developed hydrocephalus rapidly and died before weaning (6 of 36), whereas others developed ventriculomegaly without apparent changes in the shape of the skull (4 of 5). In contrast, oligo-astheno-terato-zoospermia was consistently associated with the *Hoatz*$^{-/-}$ males (33 of 33), causing infertility. The mean testicular size of the *Hoatz*$^{-/-}$ mutants was smaller compared with that of wild-type (139 $\pm$ 20.3 mg, n = 5; versus 166 $\pm$ 2.6 mg, n = 3; wet weight of one pair per animal on week 7). Sperm was collected from cauda epididymis by a swim-out protocol, revealing the mutant sperm count to be approximately 15% of wild-type values (Figure 2C). The recovery of sperm using this swim-out protocol may have been lower in the *Hoatz*$^{-/-}$ mice compared with the wild-type samples because of the lack of flagellar motility. We therefore employed another protocol in which semen in the epididymal tail was pushed out using forceps (Nagy et al., 2003). Although the semen was too viscous to accurately measure using a micropipette, the concentrations were approximately 2×10^8 and 1×10^9 cells/mL for *Hoatz*$^{-/-}$ and wild-type mice. The epididymal sperm of the *Hoatz*$^{-/-}$ mutants exhibited severe morphological defects, and their flagella were immotile (Figures 2D–2F). In contrast, the heterozygous males were fertile, although their sperm flagella were often mildly swollen, bent irregularly at the annulus, or both. Females with heterozygous or *Hoatz*$^{-/-}$ mutations were fertile (average litter sizes: 7.2 $\pm$ 2.8, n = 24, and 7.1 $\pm$ 1.9, n = 8 for heterozygous and *Hoatz*$^{-/-}$ mice, respectively), although they exhibited higher mortality rates owing to obstructed labor compared with that of wild-type (0 of 22, 4 of 13, and 2 of 8 crossings for wild-type, heterozygous, and *Hoatz*$^{-/-}$ females, respectively).

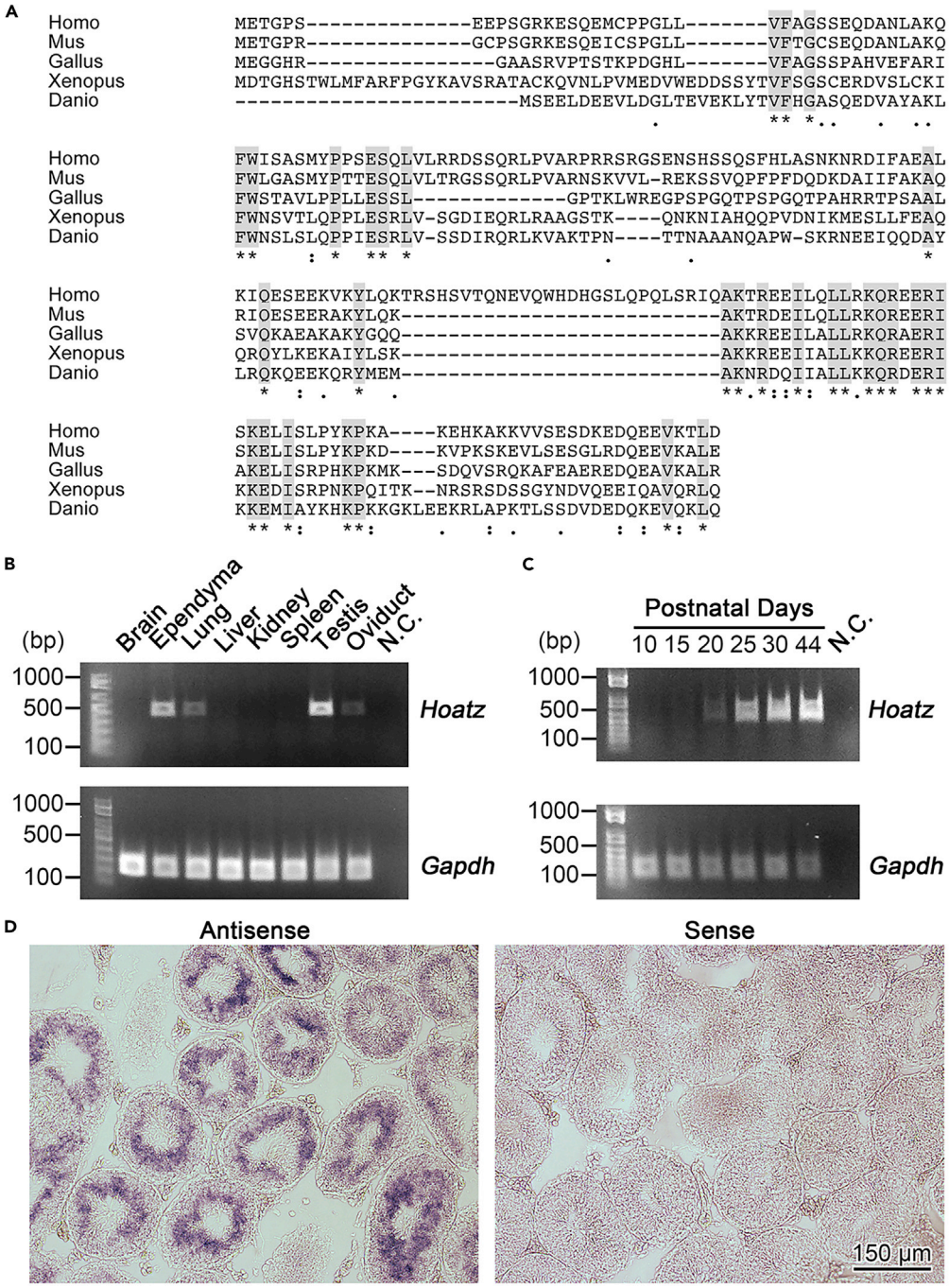

Figure 1. *Hoatzin* mRNA Is Specifically Expressed in Tissues with Motile Cilia and Flagella

(A) The amino acid sequence alignment of HOATZ with those of proteins of diverse species was generated using the MUSCLE program (Edgar, 2004).

(B) Semiquantitative reverse-transcriptase polymerase chain reaction (RT-PCR) analysis of *Hoatz* expression using RNAs extracted from the mouse brain, ependyma (primary culture), lung, liver, kidney, spleen, testis, and oviduct. N.C., negative control (minus template). *Gapdh* mRNA served as a control.

(C) Changes in mRNA expression levels of *Hoatz* during the first wave of spermatogenesis. N.C., negative control (minus template). *Gapdh* mRNA served as a control.

(D) Detection of *Hoatz* mRNA in mouse testis using RNA *in situ* hybridization. The tissue sections were incubated with antisense and sense probes. The absence of a signal in the section incubated with the sense probe indicates the specificity of the hybridization. See also Figure S1 and Video S1.

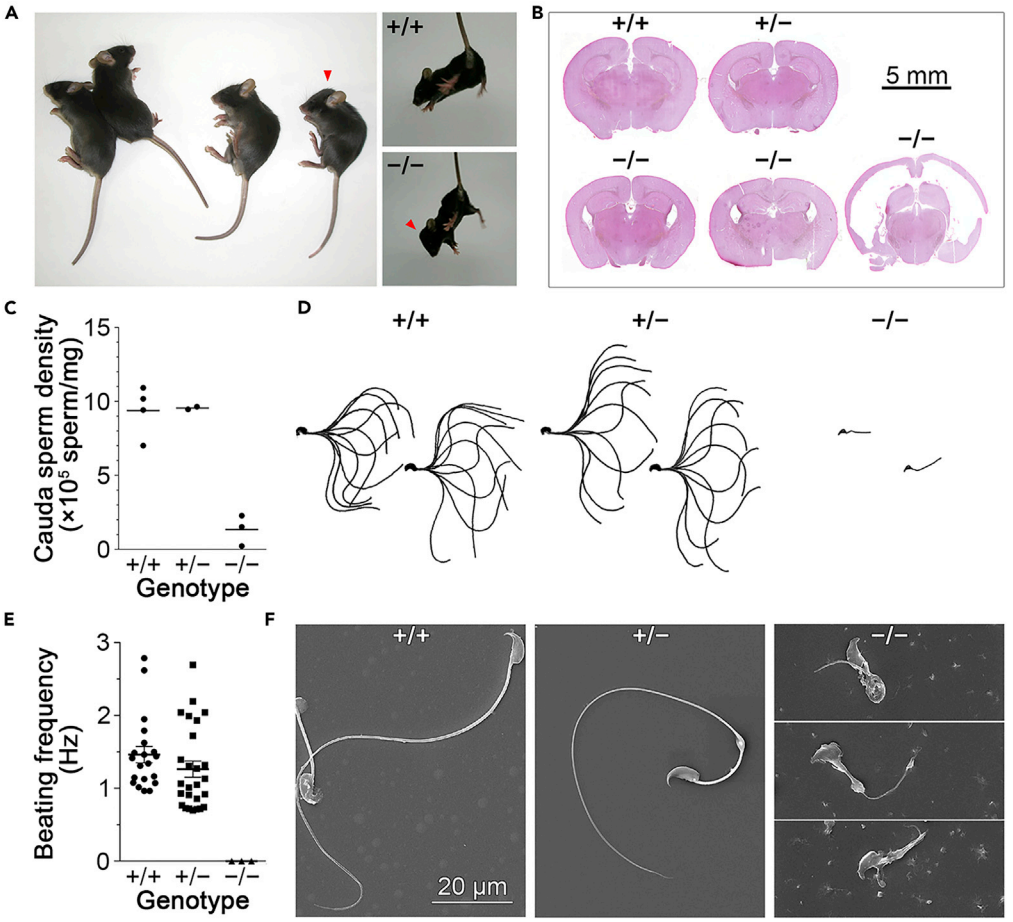

Figure 2. Knockout of *Hoatz* Causes Hydrocephalus and Oligo-Astheno-Terato-Zoospermia

(A) Four-weeks-old male littermates of *Hoatz*$^{+/-}$ heterozygous parents. One mouse with a *Hoatz*$^{-/-}$ genotype exhibited a dome-like skull (arrowhead) characteristic of hydrocephalus.

(B) H&E-stained coronal section of the brain from the 4-week-old littermates described above. Note the enlarged lateral ventricles in the three *Hoatz*$^{-/-}$ mutants compared with those of the wild-type and heterozygote.

(C) Scatterplots with median lines showing the cauda epididymal sperm density of sexually mature littermates. Note that the *Hoatz*$^{-/-}$ spermatozoa did not have motile full-length flagella (n = 4, 2, and 3 for wild-type, heterozygote, and null, respectively).

(D) High-speed video microscopy of the sperm-flagellar beating forms. We superimposed 10 frames at equal intervals representing one beating cycle.

(E) Scatterplots and the mean ± SEM showing the distributions of the sperm flagella beating frequency (n = 20, 26, and 3 for wild-type, heterozygote, and null mutant, respectively).

(F) Representative SEM images of the epididymal spermatozoa of sexually mature littermates.

See also Figure S2.

The deletion of *Hoatz* was not embryonic lethal, because *Hoatz*$^{-/-}$ mice generated from crosses with the heterozygotes were born at the expected Mendelian frequency (Figure S2H). The *Hoatz*$^{-/-}$ mice did not display laterality defects, polydactyly, polycystic kidney, or other notable abdominal organ abnormalities, indicating that the nodal and primary cilia were unaffected.

Motile Cilia Are Variably Affected by the Hoatz$^{-/-}$ Mutation

Immunohistochemical analysis of brain sections for the expression of acetylated α-tubulin (AcTub) and ADP-ribosylation factor-like 13B (ARL13B) detected some *Hoatz*$^{-/-}$ ependyma with very short or collapsed cilia, suggesting a partial defect in the generation or maintenance of cilia (Figure 3A). Furthermore, the mutant cilia appeared erect, suggesting defects in motility. To identify the nature of the motility defect,

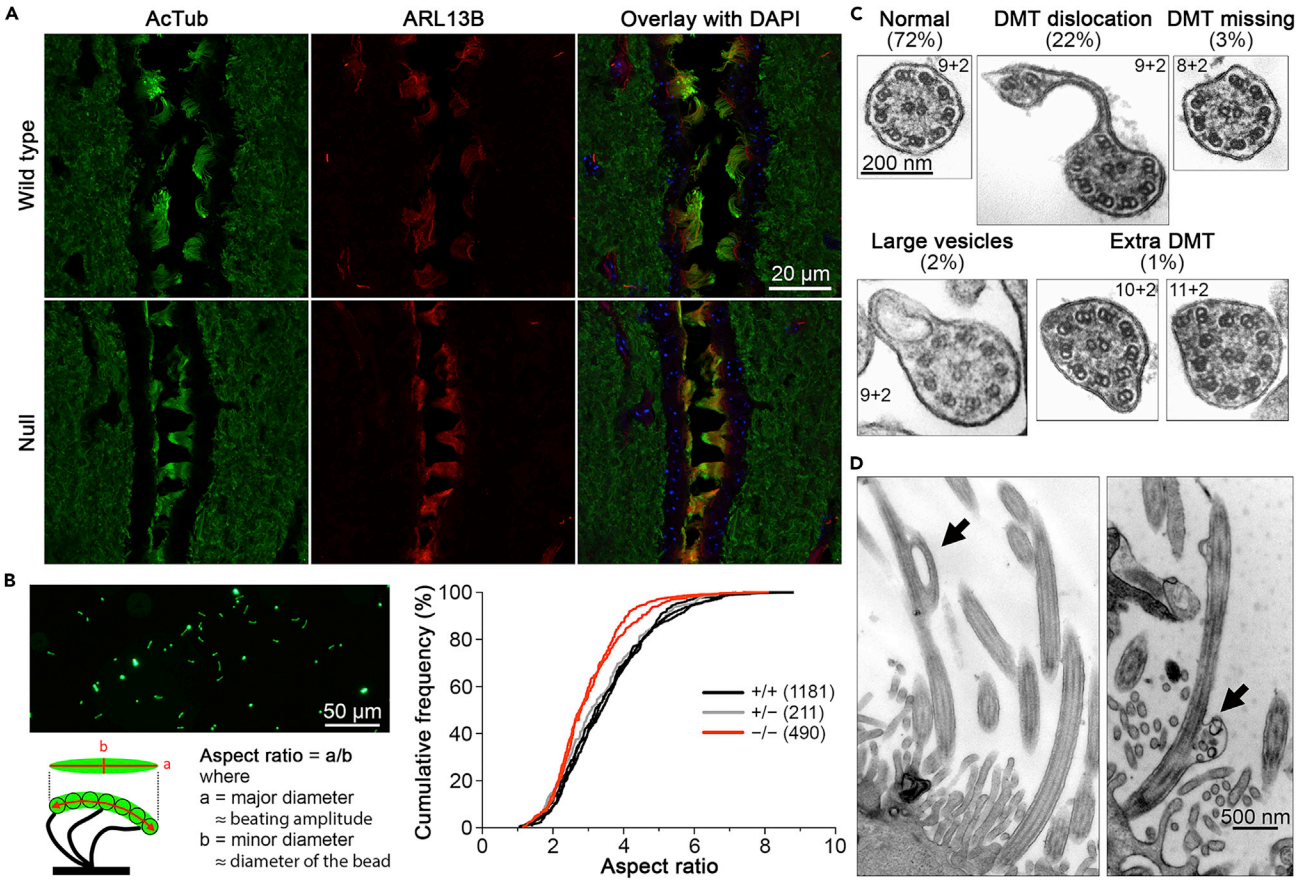

Figure 3. Motile Cilia Are Variably affected by the *Hoatz*$^{-/-}$ Mutation

(A) Confocal microscopy of the third ventricle of wild-type and *Hoatz*$^{-/-}$ mice. These coronal brain sections were incubated with antibodies against acetylated α-tubulin (green) and ARL13B (red). The nuclei were detected using DAPI (blue). Note the collapsed and straight mutant cilia. Scale bar, 20 μm.

(B) Measurement of the ciliary beating amplitude of primary cultured ependyma. Top left: representative image. The movement of motile cilia was visualized using fluorescent microbeads (exposure time, 50 ms). The major and minor axes of the best-fitting ellipse to the trace were calculated using ImageJ. Bottom left: The beating amplitude was estimated as the value of the aspect ratio (major diameter)/(minor diameter) assuming that the minor axis represents the diameter of the microbead. Right: Cumulative frequency plot of the aspect ratios of wild-type (n = 1,181), heterozygotes (n = 211), and null mutants (n = 490). $p < 0.001$, *Hoatz*$^{-/-}$ versus wild-type.

(C) Representative horizontal sections of ependymal cilia observed in *Hoatz*$^{-/-}$ mice. The cilia (n = 216) were classified into five groups. DMT, doublet microtubules.

(D) Representative longitudinal sections of the motile cilia of the ependyma of a *Hoatz*$^{-/-}$ mutant mouse showing a dislocated axonemal microtubule or an abnormal vesicle-containing small particle (black arrows).

See also Figure S3.

we performed fluorescence imaging of ependyma on glass-bottom dishes. The beating amplitudes of motile cilia of *Hoatz*$^{-/-}$ mutant cilia were smaller compared with those of wild-type and heterozygous mice (Figure 3B). Consistent with these observations, when the motility of ependymal cilia was investigated using high-speed video microscopy, the amplitude of ciliary beating (Video S1) and the beating frequency (Figure S1C) were lower compared with those of the wild-type. Stable expression of HOATZ-FLAG rescued these motility defects of the *Hoatz*$^{-/-}$ ependyma.

We next used transmission electron microscopy to observe horizontal sections of ependymal cilia of the brain ventricles. Although the majority (72%) had an apparently normal structure, defects in the arrangement of the axonemal microtubules were observed in the others (Figure 3C). The most frequent defect was outer doublet microtubule dislocations, in which one or two outer doublets were displaced from the correct position (22%). Other structural defects observed at lower frequencies were lack of one doublet microtubule (3%) and presence of extra doublet microtubules (1%). Some cilia exhibited an empty

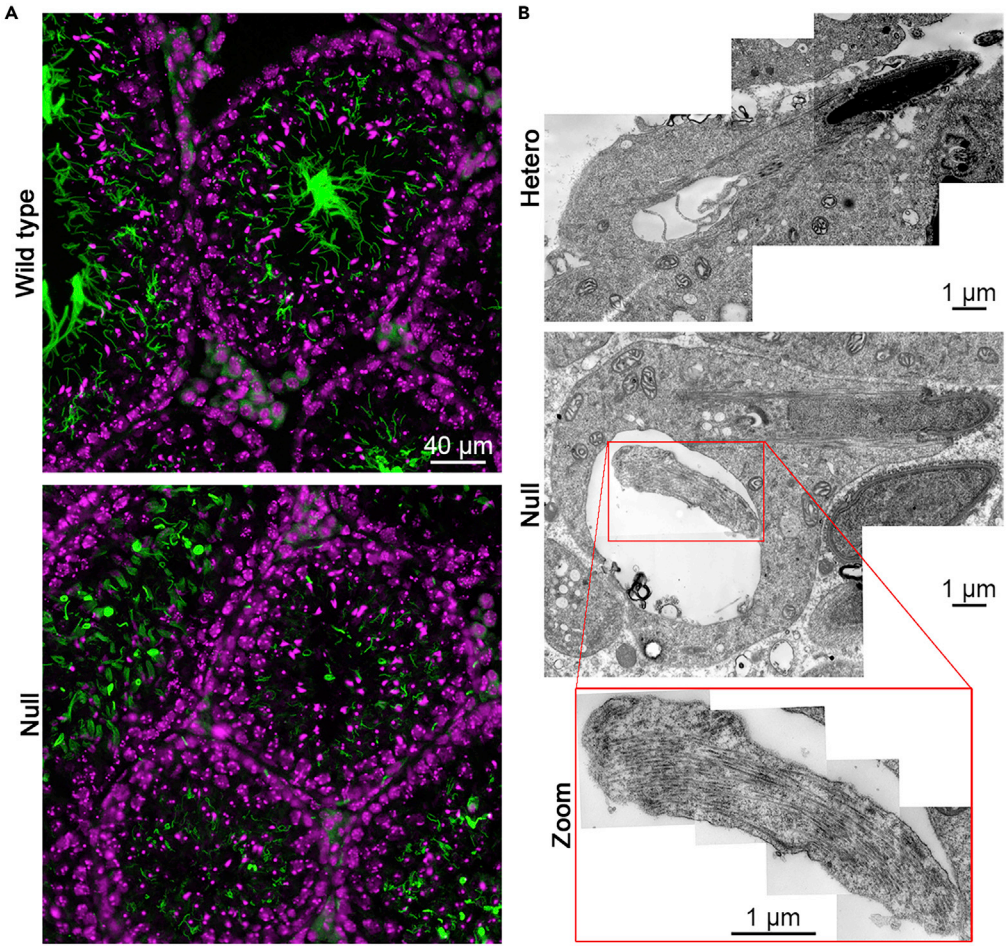

Figure 4. *Hoatz*$^{-/-}$ Seminiferous Tubules Exhibit Structural Defects

(A) Representative fluorescence microscopy images of the testes from wild-type and *Hoatz*$^{-/-}$ mice. The sections were subjected to immunohistochemistry to detect acetylated α-tubulin (green). Nuclei were detected using DAPI (pseudocolored magenta). Scale bar, 40 μm.

(B) Representative transmission electron microscopy (TEM) image tiling of spermatids undergoing cytodifferentiation in the asymptomatic heterozygous and *Hoatz*$^{-/-}$ mutants. In the *Hoatz*$^{-/-}$ mutant, a deformed flagellum contained an abnormal bundle of filaments (magnified).

See also Figures S4 and S5.

vesicle-like structure just beneath the ciliary membrane (2%); however, such vesicles were observed in the wild-type with similar frequencies and may therefore be unrelated to those of the *Hoatz*$^{-/-}$ (Figure S3A). In all cases, the central pair appeared intact. In contrast to the abnormality in the axoneme, the structures of the basal bodies, as well as the ciliary transition zone, had no apparent defects (Figure S3B). When the longitudinal sections were investigated, we observed abnormal cilia with a partial dislocation of outer doublet microtubules, consistent with the above observation (Figure 3C), or a vesicle containing heterogeneous particles (Figure 3D). Together, these data demonstrate that the mutant ependymal cilia had structural defects in the outer doublet microtubules, suggesting that this may cause a reduced beating amplitude.

We next conducted immunohistochemical analyses to identify structural defects of sperm flagella. Expression of AcTub by the *Hoatz*$^{-/-}$ mutant testis showed the lack of fully developed flagella in the lumen of the seminiferous tubules (Figure 4A). We adopted a semiquantitative numerical scoring system recommended by the OECD guidelines for the histopathological evaluation of the male reproductive system (Creasy, 2008). We assigned grade 5 (severe), because the *Hoatz*$^{-/-}$ testes lacked detectable luminal flagellar bundles in all seminiferous tubules (0 of 408 tubules, n = 4 sections), in contrast to wild-type

(295 of 312 tubules, n = 2 sections). Although short flagella (approximately ≤20 μm) were present, the number and the fluorescence intensity were significantly less compared with those of wild-type. Instead, brush-like structures, presumed to be the manchette (Lehti and Sironen, 2016), as well as curled aggregates, exhibited strong staining.

Transmission electron microscopy of the seminiferous tubules demonstrated that the flagella of the *Hoatz*$^{-/-}$ mutant spermatids undergoing cytodifferentiation often had abnormal fibrous materials with a diameter (approximately 24 nm) resembling that of singlet microtubules, instead of the well-organized axoneme (Figures 4B and S4). Accessory structures such as outer dense fibers, the fibrous sheath in the principal piece, and the spiral mitochondria in the midpiece were infrequently observed. Instead, many abnormal vesicles were observed in the cytoplasm. In early-phase spermatids with round nuclei, long developing flagella with an apparently intact axoneme without accessory structures were detected (data not shown), consistent with the immunohistochemical analysis that detected some short flagella. Together, these ultrastructural abnormalities indicate that the mutant spermatids elongated but did not maintain the axoneme, leading to severe destruction of the flagella.

The ultrastructures of motile cilia in the tracheal epithelia were investigated. Unlike those in ependyma or spermatids, the mutant axoneme was intact (Figure S5). Occasionally, blebs of the ciliary membrane were observed in distal sections.

HOATZ Interacts with Enolase 4

Having confirmed the abnormalities in the ependymal cilia and sperm flagella of the *Hoatz*$^{-/-}$ mutant, the molecular function of HOATZ was investigated. To determine if HOATZ serves as a structural component of mature sperm flagella that confers structural integrity, we determined the levels of HOATZ and AcTub expressed by wild-type testes and cauda epididyma (Figure 5A). AcTub was detected at a high level in an epididymal lysate (Figure 5A), consistent with the massive amount of mature sperm stored in the duct (Wang, 2003). In contrast, HOATZ was predominantly expressed in the testis, but at significantly lower levels in the epididymis, consistent with those of intraflagellar transport (IFT) proteins (San Agustin et al., 2015). These data indicate that HOATZ is not a structural component of sperm flagella and may contribute to the formation of motile cilia and flagella.

To investigate the effects of the *Hoatz* knockout on the ciliogenesis machinery of the Bardet-Biedl syndrome complex (BBSome) and the IFT complex, testes from the wild-type and *Hoatz*$^{-/-}$ mice were lysed, fractionated using sucrose density gradient centrifugation (Nachury et al., 2007), and subjected to western blot analyses to detect BBS7, IFT88, and IFT140. The levels and integrities of the BBSome, IFT-B, and IFT-A complexes were unaffected in the absence of HOATZ (Figure 5B). Furthermore, immunoprecipitation analysis of wild-type lysates failed to detect a direct interaction between HOATZ and BBS7 or IFT88 (data not shown).

In the testis homogenate, HOATZ (19 kDa) sedimented significantly faster through a sucrose gradient compared with chymotrypsinogen A (2.6S, 25 kDa) and was distributed over a broad range of fractions, including those containing apoferritin (17.6S, 490 kDa) (Figure 5B). In contrast, when a whole-cell lysate of 293T cells overexpressing recombinant HOATZ-FLAG was similarly analyzed, ectopically expressed HOATZ was enriched at the top of the gradient as expected according to its molecular mass, suggesting it existed as a free monomer (Figure S6A). These data suggest that HOATZ associated with tissue-specific proteins, likely those involved in motile ciliogenesis.

To identify the binding partners of HOATZ, testis lysates were immunoprecipitated with the anti-HOATZ antibody (Figure 5C). Liquid chromatography-mass spectrometry identified 253 and 260 proteins in the wild-type and the *Hoatz*$^{-/-}$ mutant samples, respectively (Data S1). We selected for further study those that were specifically or more frequently (>3 fold-higher peptide-to-spectrum matches) detected in the wild-type sample. In the resulting new dataset containing 27 proteins, HOATZ (C11ORF88 homolog) was ranked as the second most frequently detected protein (Data S2). We detected the tubulins TUBB5, TUBB3, and TUBA3A; heat shock proteins HSPA8, HSPA1L, and HSPA4L; and deleted in lung and esophageal cancer protein 1 (DLEC1, also known as CFAP81) as candidate HOATZ-binding proteins. We also detected RNA-binding proteins such as apoptotic chromatin condensation inducer 1 (ACIN1), RNA binding protein with serine rich domain 1 (RNPS1), DEAH-box helicase 15 (DHX15), small nuclear ribonucleoprotein U4/U6.U5 subunit 27 (SNRNP27), and arginine and

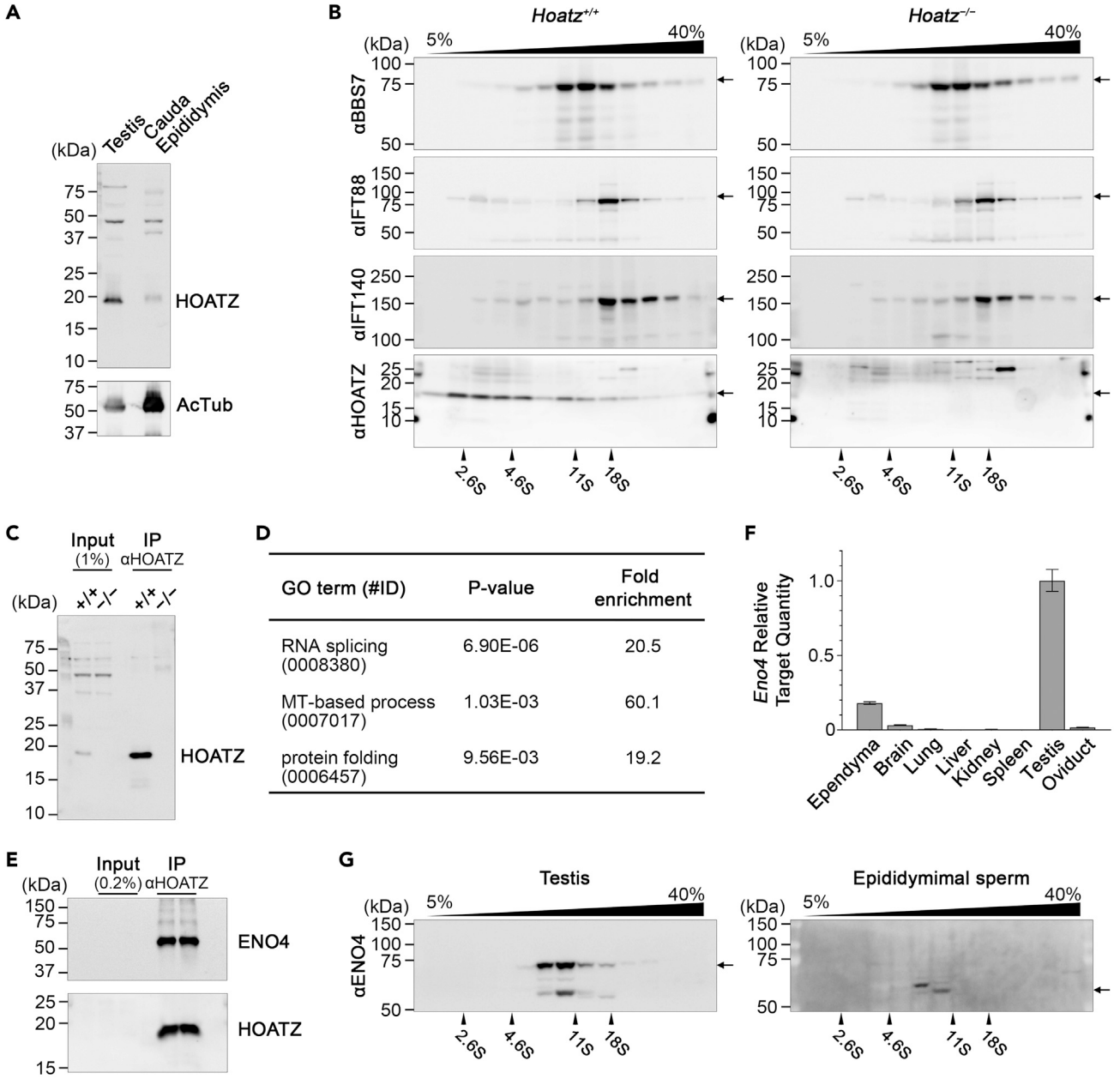

Figure 5. HOATZ Interacts with Enolase 4

(A) Comparison of endogenous HOATZ levels between testis and cauda epididymis containing mature sperm in wild-type mice. AcTub served as a marker of cilia and flagella.

(B) Comparison of BBS7, IFT88, and IFT140 levels between wild-type and *Hoatz*$^{-/-}$ mouse testes. Tissue homogenates were fractionated using sucrose density gradient centrifugation and concentrated using TCA precipitation. The levels of BBS7, IFT88, IFT140, and HOATZ were analyzed using western blotting with the respective antibodies.

(C) Immunoprecipitation for shotgun proteomics. Testis homogenates from wild-type and *Hoatz*$^{-/-}$ mice were incubated with a rabbit polyclonal anti-HOATZ IgG cross-linked to magnetic beads, and the eluates were subjected to LC-MS to detect potential HOATZ-binding proteins. HOATZ levels in the eluates were determined using western blotting.

(D) Gene Ontology analysis of proteins eluted from of the anti-HOATZ immunoprecipitates. A dataset comprising 27 HOATZ-associated proteins was analyzed using the DAVID server (Huang et al., 2009).

(E) Western blot analysis of ENO4 eluted from immunoprecipitates.

Figure 5. *Continued*

(F) Real-time PCR analysis of *Eno4* mRNA levels using the comparative C_T method. The $\Delta\Delta C_T$ values were calculated using *B2m* as an endogenous reference and testis as a calibrator. The data are expressed as the mean, minimum, and maximum relative target quantities (n = 3).

(G) Western blot analysis of ENO4 levels in the homogenates of testis and cauda epididymis containing mature sperm.

See also Figure S6 and Data S1 and S2.

serine rich coiled-coil 1 (RSRC1) whose tissue expression patterns and functions do not correlate with motile cilia and flagella. Gene Ontology analysis of these proteins suggested that HOATZ is involved in the biological processes of RNA splicing, microtubule-based process, and protein folding (Figure 5D). This dataset included metabolic enzymes involved in the pay-off phase of glycolysis, enolase 4 (ENO4) and glyceraldehyde-3-phosphate dehydrogenase (GAPDH) (Data S2). To assess an interaction between HOATZ and ENO4, testis lysates were immunoprecipitated using the anti-HOATZ antibody as described above, and the eluates were subjected to western blot analysis. As we expected, ENO4 was enriched in the eluate along with HOATZ (Figure 5E).

We further studied ENO4, because male *Eno4* KO mice are infertile because of a severe defect of spermatogenesis, similar to that of the *Hoatz*$^{-/-}$ phenotype described above (Nakamura et al., 2013). Real-time PCR analysis confirmed that *Eno4* mRNA was expressed at high levels in testis, to some extent in the ependyma (Figure 5F), but at low levels in lung and oviduct. Western blot analysis of wild-type tests homogenates fractionated using sucrose density gradient centrifugation demonstrated that ENO4 was enriched in fractions of approximately 10S, overlapping only partially with HOATZ (Figure 5G). The difference in the distributions of ENO4 and HOATZ in the sucrose density gradient suggested that these proteins may not exclusively associate. Furthermore, western blotting detected a major band at approximately 70 kDa and a minor band at approximately 60 kDa. In contrast, the 70-kDa band was not detected in wild-type cauda epididyma, although the 60 kDa was (Figure 5G). We therefore speculated that ENO4 may undergo processing before its transport to mature flagella.

HOATZ Mediates the Processing of ENO4

Western blot analysis of sucrose density gradients showed an increase of ENO4, particularly that of its 70-kDa form, in the *Hoatz*$^{-/-}$ mutant (Figure 6A). To directly compare ENO4 levels between the *Hoatz*$^{-/-}$ and wild-type mice, the ENO4-positive fractions from both genotypes were loaded on the same gel and blotted on the same membrane to compare their signal intensities (arbitrary units) relative to that of an internal standard (actin) (Figure 6B). The differences were statistically significant ($p = 0.02$, $n = 4$). When the testes sections were subjected to immunohistochemical analysis, ENO4 was detected in small puncta in the cytoplasm of haploid spermatids of the wild-type and mutant. Furthermore, the tubules of the *Hoatz*$^{-/-}$ mutant exhibited many puncta compared with those of the wild-type during seminiferous stages V–VII (Figure 6C). Similarly, when primary cultured ependyma were homogenized and fractionated on sucrose density gradients, western blot analysis detected an increase in ENO4 levels in the *Hoatz*$^{-/-}$ mutant (Figure S6B), strongly suggesting that HOATZ mediated the maturation of ENO4.

DISCUSSION

Here our characterization of the cilia-related gene *Hoatz* (*4833427G06Rik*) sheds light on the molecular mechanism of motile ciliogenesis that is particularly important in spermatids and the ependyma. *Hoatz* was first identified as one of 99 mouse cilia-related genes, according to its tissue expression pattern (McClintock et al., 2007). Microarray analysis shows that in zebrafish, *hoatz* (*C11orf88* homolog) is among the top 15 upregulated genes in testis (Small et al., 2009). Our RT-PCR data (Figure 1) are consistent with these reports. *Hoatz* is a candidate *Foxj1*–dependent factor in the lung, but not for *Noto* effectors in the embryonic node (Stauber et al., 2017), which agrees with our observation that *Hoatz*$^{-/-}$ mice had no detectable L-R defect. However, *Hoatz*$^{-/-}$ mice exhibited severe defects in spermatogenesis, leading to infertility and varying degrees of hydrocephalus (Figures 2, 3, and 4). The results of our present biochemical analyses (Figures 5 and 6) lead us to propose that HOATZ mediates the maturation of the glycolytic enzyme ENO4, thus contributing to the translocation of the latter during motile ciliogenesis and flagellar genesis (Figure 7).

Enolase catalyzes the conversion of 2-phosphoglycerate to phosphoenolpyruvate in the pay-off phase of glycolysis. Vertebrate genomes encode *Eno1–4*. *Eno1* is expressed ubiquitously, and *Eno2* and *Eno3* are specifically expressed in neurons and muscles (skeletal and heart), respectively (Isgrò et al., 2015; Merkulova et al., 1997), suggesting the importance of the latter two isoforms in ATP production in highly energy-demanding cell types. Similarly, *Eno4* is specifically expressed by spermatogenic cells and has

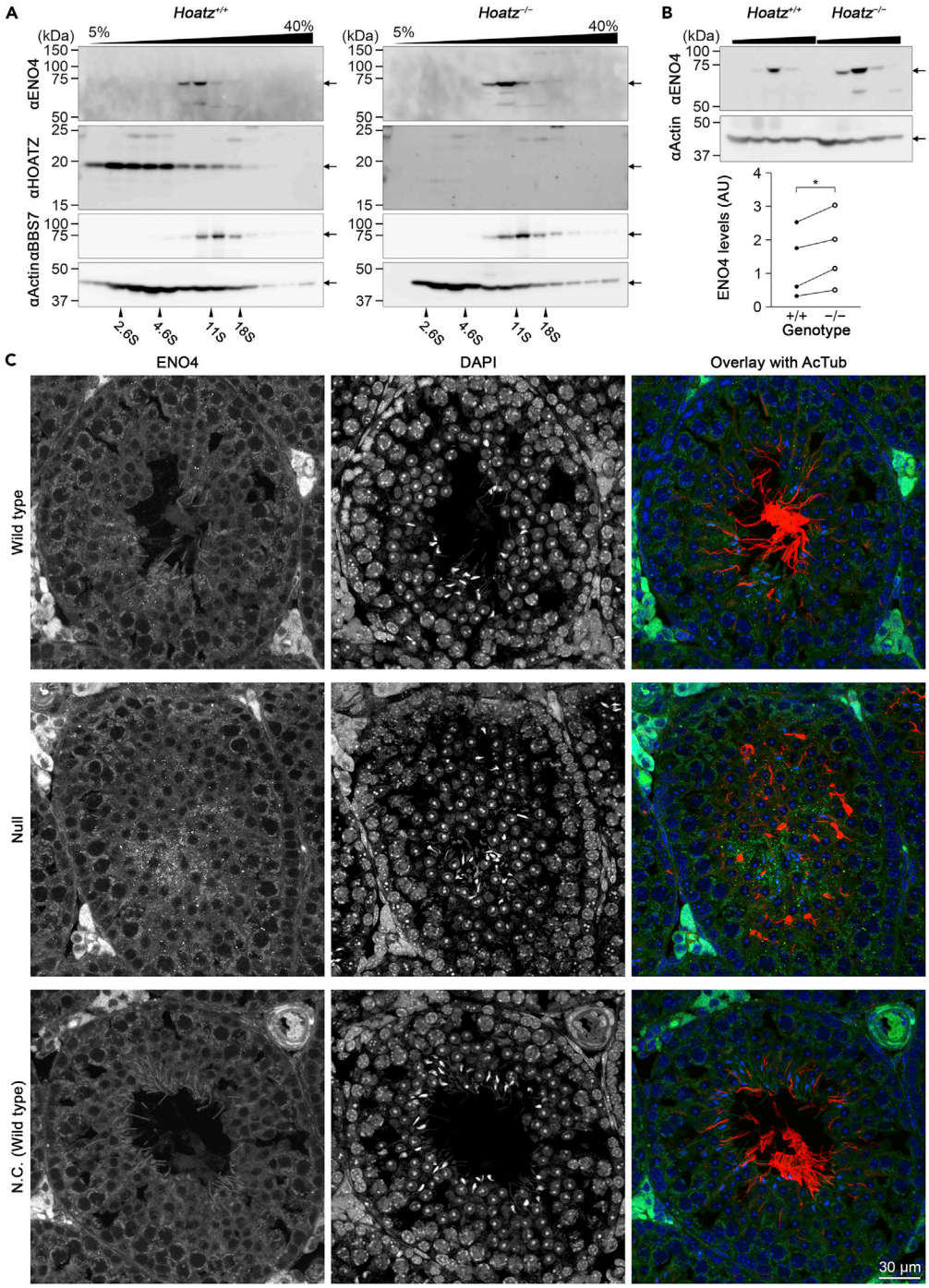

Figure 6. Abnormal Accumulation of ENO4 in the Testes of *Hoatz*$^{-/-}$ Mice

(A) Western blot analysis of ENO4 levels in wild-type and the *Hoatz*$^{-/-}$ mouse testes. The tissue homogenates were fractionated using sucrose density gradient centrifugation, and the levels of ENO4, HOATZ, BBS7, and actin isoforms (loading control) were determined.

(B) Top: Fractions containing ENO4 from wild-type and *Hoatz*$^{-/-}$ mice were resolved on the same gel. Bottom: Quantification of the immunoreactive bands. The data are expressed as relative values (arbitrary unit) to actin (paired t test, *p = 0.02, n = 4).

(C) Representative confocal images of stages V–VII seminiferous tubules, ENO4 (green), AcTub (red), and DAPI (blue). As a negative control (N.C.), a wild-type section was incubated with normal rabbit IgG and mouse anti-AcTub. Note the accumulation of ENO4-positive puncta at the luminal side of the *Hoatz*$^{-/-}$ seminiferous tubule. Scale bar, 30 μm.

See also Figure S6.

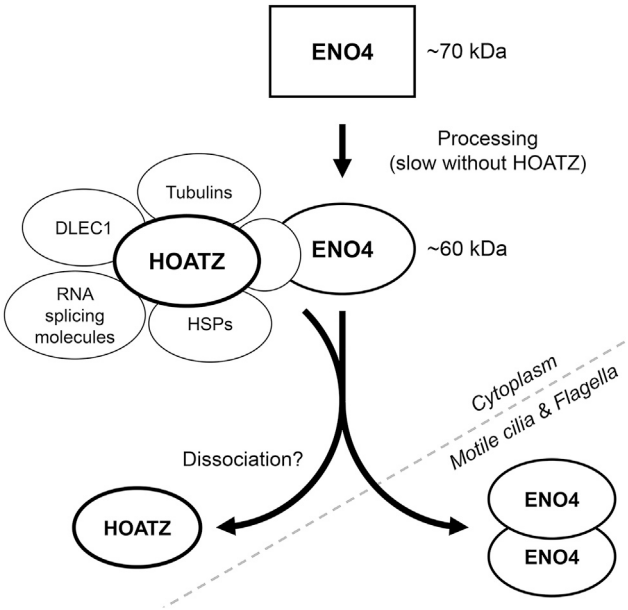

Figure 7. Diagram Showing the Proposed Function of HOATZ

ENO4 is synthesized as an approximately 70-kDa precursor, which then undergoes proteolytic cleavage to an approximately 60-kDa enzyme. HOATZ associates directly or indirectly with ENO4 to mediate this process.

been associated with a previously characterized sperm-specific enolase activity of ENO-S (Edwards and Grootegoed, 1983; Nakamura et al., 2013). Here, the expression of *Eno4* mRNA and protein was detected in spermatids and ependyma (Figures 5, 6, S6B). Thus, these cells may serve as a third energy-demanding cell type that requires specific enolases. Although previous proteomic analyses of mature human sperm detected ENO1 (Martínez-Heredia et al., 2006) and ENO4 (Vandenbrouck et al., 2016), which may indicate functional redundancy and compensation, the KO phenotype of *Eno4* mice demonstrates the requirement of *Eno4* in the formation of sperm flagella formation (Nakamura et al., 2013).

Eno4 and *Hoatz* are conserved only in vertebrates, indicating that they may have been acquired to accomplish motile ciliogenesis specific to vertebrates. Interestingly, spermatids and ependyma reside in anatomical regions protected by the blood-testis and blood-brain barriers, respectively, indicating their requirement in tissues in which the nutrient supply from circulating blood is strictly regulated. However, although ENO1–3 share the same catalytic site structure, which is evolutionarily conserved (López-López et al., 2018), ENO4 has several substitutions in those critical residues, raising concerns about the enolase activity (K. Narita, Unpublished Data). As enolases form homo- and heterodimers (Ueta et al., 2004), ENO4 may heterodimerize with ENO1 to act together with HOATZ as its transporter into motile cilia and flagella. Furthermore, ENO4 may bind 2-phosphoglycerate to protect this high-energy substrate from degradation. In addition, functions other than glycolysis are associated with ENO1 protein and its fragment (Ji et al., 2016; Lung et al., 2010). Similarly, ENO4 may mediate multiple functions to participate in motile ciliogenesis independent of glycolytic activity.

Interestingly, although *Eno4* KO mice exhibited severe malformations of the spermatids of the cauda epididymis, only minor abnormalities were apparent in the histology and ultrastructure of the testis, with no indication of hydrocephalus (Nakamura et al., 2013). Although the highly analogous morphological defects of the *Hoatz*- and *Eno4*-null spermatids support the conclusion that they function in the same biological process, the KO phenotype of the former was more severe, suggesting that the function of HOATZ is not limited to processing ENO4. The potential HOATZ-interacting proteins identified here (Data S2) suggest the involvement of HOATZ in RNA splicing, microtubule-based processes, and protein folding. These possibilities will be addressed in the future.

In *Chlamydomonas* flagella, axonemal enolase forms the central pair complex CPC1, a component of the C1b projection, together with HSP70A and other proteins (Mitchell, 2005). Furthermore, recent proteomic analysis of the central pair of *Chlamydomonas* flagella identified DLEC1-homolog FAP81 as a component

of the C1a projection (Zhao et al., 2019). The amino acid sequences of *Chlamydomonas* enolase are 67% and 26% identical to those of mouse ENO1 and ENO4, respectively, and our present shotgun proteomic analysis identified enolase, heat shock proteins, tubulins, and DLEC1 as potential HOATZ-interacting proteins (Data S2). Although our ultrastructural analysis of the *Hoatz*$^{-/-}$ mutant ependymal cilia demonstrates instabilities of the outer doublets rather than the central pair (Figure 3), HOATZ may contribute to the formation of the central apparatus in vertebrates. Clearly, further investigation is required to identify the functional relationships among ENO1, ENO4, and HOATZ that mediate vertebrate motile ciliogenesis.

Our present data demonstrate that *Hoatz* is a ciliopathy gene of mice. On the other hand, there are no reports of mutations in *HOATZ* that are associated with human diseases. This may be explained by the small size of the exons, which decreases the probability of random mutagenesis and its autosomal recessive mode of inheritance. Similar to *HOATZ*, other uncharacterized small genes may have significant biological functions that are not associated with human pathology (Pauli et al., 2014). Moreover, small genes encoding proteins comprising fewer than 100 amino acid residues are difficult to annotate (Pauli et al., 2015). Recent advances in the genome editing technology promise to enhance our understanding of small, nonannotated genes.

Limitations of the Study

We are checking a presumed null allele with a novel antibody and consider this as a limitation of the study. The specificity of the antibody has been confirmed using the strain #3. The strains #1 and #2 had been cryopreserved using heterozygous sperm because of the cost required to maintain the mice.

METHODS

All methods can be found in the accompanying Transparent Methods supplemental file.

DATA AND CODE AVAILABILITY

The datasets supporting the current study have not been deposited in a public repository because of large file size but are available from the corresponding author on request.

SUPPLEMENTAL INFORMATION

Supplemental Information can be found online at https://doi.org/10.1016/j.isci.2020.100992.

ACKNOWLEDGMENTS

We thank Prof. Teruhiko Wakayama for generating the KO mouse, Dr. Osamu Kutomi for helping with RNA *in situ* hybridization, Prof. Ryohei Kato and Mamiko Otagiri for preparing tissue sections, Kazuko Sawanobori for secretarial assistance, and Edanz Group (www.edanzediting.com/ac) for editing a draft of this manuscript. This research was supported by JSPS KAKENHI (Grant Numbers JP26440094 and JP18K06824 to K.N.; JP17K08511 to S.T.) and the Japan Spina Bifida & Hydrocephalus Research Foundation (to K.N.).

AUTHOR CONTRIBUTIONS

Conceptualization, K.N.; Methodology, K.N. and M.O.; Validation, K.N.; Formal Analysis, K.N.; Investigation, K.N. and H.K-H; Resources, K.N. and H.N.; Data Curation, K.N. and H.K-H; Writing – Original Draft Preparation, K.N.; Writing – Review and Editing, K.N. and S.T.; Visualization, K.N.; Supervision, K.N., M.O., and S.T.; Project Administration, K.N. and S.T.; Funding Acquisition, K.N. and S.T.

DECLARATION OF INTERESTS

The authors declare no competing interests.

Received: August 25, 2019
Revised: January 13, 2020
Accepted: March 12, 2020
Published: April 24, 2020

REFERENCES

Berg, J., Tymoczko, J., and Stryer, L. (2011). Glycolysis and gluconeogenesis. In Biochemistry, 7th Edition (W. H. Freeman and Company), pp. 469–513.

Choksi, S.P., Lauter, G., Swoboda, P., and Roy, S. (2014). Switching on cilia: transcriptional networks regulating ciliogenesis. Development *141*, 1427–1441.

Creasy, D. (2008). Male reproductive system. Endocr. Disrupt. A Guid. Doc. Histol. Eval. Endocr. Reprod. Tests, 27–56.

Edgar, R.C. (2004). MUSCLE: multiple sequence alignment with high accuracy and high throughput. Nucleic Acids Res. *32*, 1792–1797.

Edwards, Y.H., and Grootegoed, J.A. (1983). A sperm-specific enolase. J. Reprod. Fertil. *68*, 305–310.

Gerdes, J.M., Davis, E.E., and Katsanis, N. (2009). The vertebrate primary cilium in development, homeostasis, and disease. Cell *137*, 32–45.

Hirokawa, N., Tanaka, Y., Okada, Y., and Takeda, S. (2006). Nodal flow and the generation of left-right asymmetry. Cell *125*, 33–45.

Huang, D.W., Sherman, B.T., and Lempicki, R.A. (2009). Systematic and integrative analysis of large gene lists using DAVID bioinformatics resources. Nat. Protoc. *4*, 44–57.

Isgrò, M.A., Bottoni, P., and Scatena, R. (2015). Neuron-specific enolase as a biomarker: biochemical and clinical aspects. Adv. Exp. Med. Biol. *867*, 125–143.

Ji, H., Wang, J., Guo, J., Li, Y., Lian, S., Guo, W., Yang, H., Kong, F., Zhen, L., Guo, L., et al. (2016). Progress in the biological function of alpha-enolase. Anim. Nutr. *2*, 12–17.

Khan, S., and Scholey, J.M. (2018). Assembly, functions and evolution of archaella, flagella and cilia. Curr. Biol. *28*, R278–R292.

Lehti, M.S., and Sironen, A. (2016). Formation and function of the manchette and flagellum during spermatogenesis. Reproduction *151*, R43–R54.

Lin, J., Yin, W., Smith, M.C., Song, K., Leigh, M.W., Zariwala, M.A., Knowles, M.R., Ostrowski, L.E., and Nicastro, D. (2015). Cryo-electron tomography reveals ciliary defects underlying human RSPH1 primary ciliary dyskinesia. Nat. Commun. *5*, 5727.

López-López, M.de J., Rodríguez-Luna, I.C., Lara-Ramírez, E.E., López-Hidalgo, M., Benítez-Cardoza, C.G., and Guo, X. (2018). Biochemical and biophysical characterization of the enolase from *Helicobacter pylori*. Biomed. Res. Int. *2018*, 9538193.

Lung, J., Liu, K.J., Chang, J.Y., Leu, S.J., and Shih, N.Y. (2010). MBP-1 is efficiently encoded by an alternative transcript of the ENO1 gene but post-translationally regulated by proteasome-dependent protein turnover. FEBS J. *277*, 4308–4321.

Martínez-Heredia, J., Estanyol, J.M., Ballescà, J.L., and Oliva, R. (2006). Proteomic identification of human sperm proteins. Proteomics *6*, 4356–4369.

McClintock, T.S., Glasser, C.E., Bose, S.C., and Bergman, D.A. (2007). Tissue expression patterns identify mouse cilia genes. Physiol. Genomics *32*, 198–206.

Merkulova, T., Lucas, M., Jabet, C., Lamandé, N., Rouzeau, J.-D., Gros, F., Lazar, M., and Keller, A. (1997). Biochemical characterization of the mouse muscle-specific enolase: developmental changes in electrophoretic variants and selective binding to other proteins. Biochem. J. *323*, 791–800.

Mitchell, B.F. (2005). ATP production in *Chlamydomonas reinhardtii* flagella by glycolytic enzymes. Mol. Biol. Cell *16*, 4509–4518.

Nachury, M.V., Loktev, A.V., Zhang, Q., Westlake, C.J., Peränen, J., Merdes, A., Slusarski, D.C., Scheller, R.H., Bazan, J.F., Sheffield, V.C., et al. (2007). A core complex of BBS proteins Cooperates with the GTPase Rab8 to promote ciliary membrane biogenesis. Cell *129*, 1201–1213.

Nagy, A., Vintersten, K., and Behringer, R. (2003). Manipulating the Mouse Embryo: A Laboratory Manual, 3rd Edition (Cold Spring Harbor Laboratory Press).

Nakamura, N., Dai, Q., Williams, J., Goulding, E.H., Willis, W.D., Brown, P.R., and Eddy, E.M. (2013). Disruption of a spermatogenic cell-specific mouse enolase 4 (Eno4) gene causes sperm structural defects and male infertility. Biol. Reprod. *88*, 90.

Olcese, C., Patel, M.P., Shoemark, A., Kiviluoto, S., Legendre, M., Williams, H.J., Vaughan, C.K., Hayward, J., Goldenberg, A., Emes, R.D., et al. (2017). X-linked primary ciliary dyskinesia due to mutations in the cytoplasmic axonemal dynein assembly factor PIH1D3. Nat. Commun. *8*, 14279.

Omran, H., Kobayashi, D., Olbrich, H., Tsukahara, T., Loges, N.T., Hagiwara, H., Zhang, Q., Leblond, G., O'Toole, E., Hara, C., et al. (2008). Ktu/PF13 is required for cytoplasmic pre-assembly of axonemal dyneins. Nature *456*, 611–616.

Pauli, A., Norris, M.L., Valen, E., Chew, G.L., Gagnon, J.A., Zimmerman, S., Mitchell, A., Ma, J., Dubrulle, J., Reyon, D., et al. (2014). Toddler: an embryonic signal that promotes cell movement via apelin receptors. Science *343*, 1248636.

Pauli, A., Valen, E., and Schier, A.F. (2015). Identifying (non-)coding RNAs and small peptides: challenges and opportunities. BioEssays *37*, 103–112.

Pazour, G.J., Agrin, N., Leszyk, J., and Witman, G.B. (2005). Proteomic analysis of a eukaryotic cilium. J. Cell Biol. *170*, 103–113.

San Agustin, J.T., Pazour, G.J., and Witman, G.B. (2015). Intraflagellar transport is essential for mammalian spermiogenesis but is absent in mature sperm. Mol. Biol. Cell *26*, 4358–4372.

Small, C.M., Carney, G.E., Mo, Q., Vannucci, M., and Jones, A.G. (2009). A microarray analysis of sex- and gonad-biased gene expression in the zebrafish: evidence for masculinization of the transcriptome. BMC Genomics *10*, 579.

Snell, W.J., Pan, J., and Wang, Q. (2004). Cilia and flagella revealed: from flagellar assembly in Chlamydomonas to human obesity disorders. Cell *117*, 693–697.

Stauber, M., Weidemann, M., Dittrich-Breiholz, O., Lobschat, K., Alten, L., Mai, M., Beckers, A., Kracht, M., and Gossler, A. (2017). Identification of FOXJ1 effectors during ciliogenesis in the foetal respiratory epithelium and embryonic left-right organiser of the mouse. Dev. Biol. *423*, 170–188.

Ueta, H., Nagasawa, H., Oyabu-Manabe, Y., Toida, K., Ishimura, K., and Hori, H. (2004). Localization of enolase in synaptic plasma membrane as an $\alpha\gamma$ heterodimer in rat brain. Neurosci. Res. *48*, 379–386.

Vandenbrouck, Y., Lane, L., Carapito, C., Duek, P., Rondel, K., Bruley, C., Macron, C., Gonzalez De Peredo, A., Couté, Y., Chaoui, K., et al. (2016). Looking for missing proteins in the proteome of human spermatozoa: an update. J. Proteome Res. *15*, 3998–4019.

Wang, Y. (2003). Epididymal sperm count. In Current Protocols in Toxicology, M.D. Maines, ed. (John Wiley and Sons), pp. 16.–6.

Zariwala, M.A., Knowles, M.R., and Omran, H. (2006). Genetic defects in ciliary structure and function. Annu. Rev. Physiol. *69*, 423–450.

Zhao, L., Hou, Y., Picariello, T., Craige, B., and Witman, G.B. (2019). Proteome of the central apparatus of a ciliary axoneme. J. Cell Biol. *218*, 2051–2070.

Zimmermann, C., Stévant, I., Borel, C., Conne, B., Pitetti, J.L., Calvel, P., Kaessmann, H., Jégou, B., Chalmel, F., and Nef, S. (2015). Research resource: the dynamic transcriptional profile of sertoli cells during the progression of spermatogenesis. Mol. Endocrinol. *29*, 627–642.

iScience, Volume *23*

Supplemental Information

Discovery of a Vertebrate-Specific Factor that Processes Flagellar Glycolytic Enolase during Motile Ciliogenesis

Keishi Narita, Hiroaki Nagatomo, Hiroko Kozuka-Hata, Masaaki Oyama, and Sen Takeda

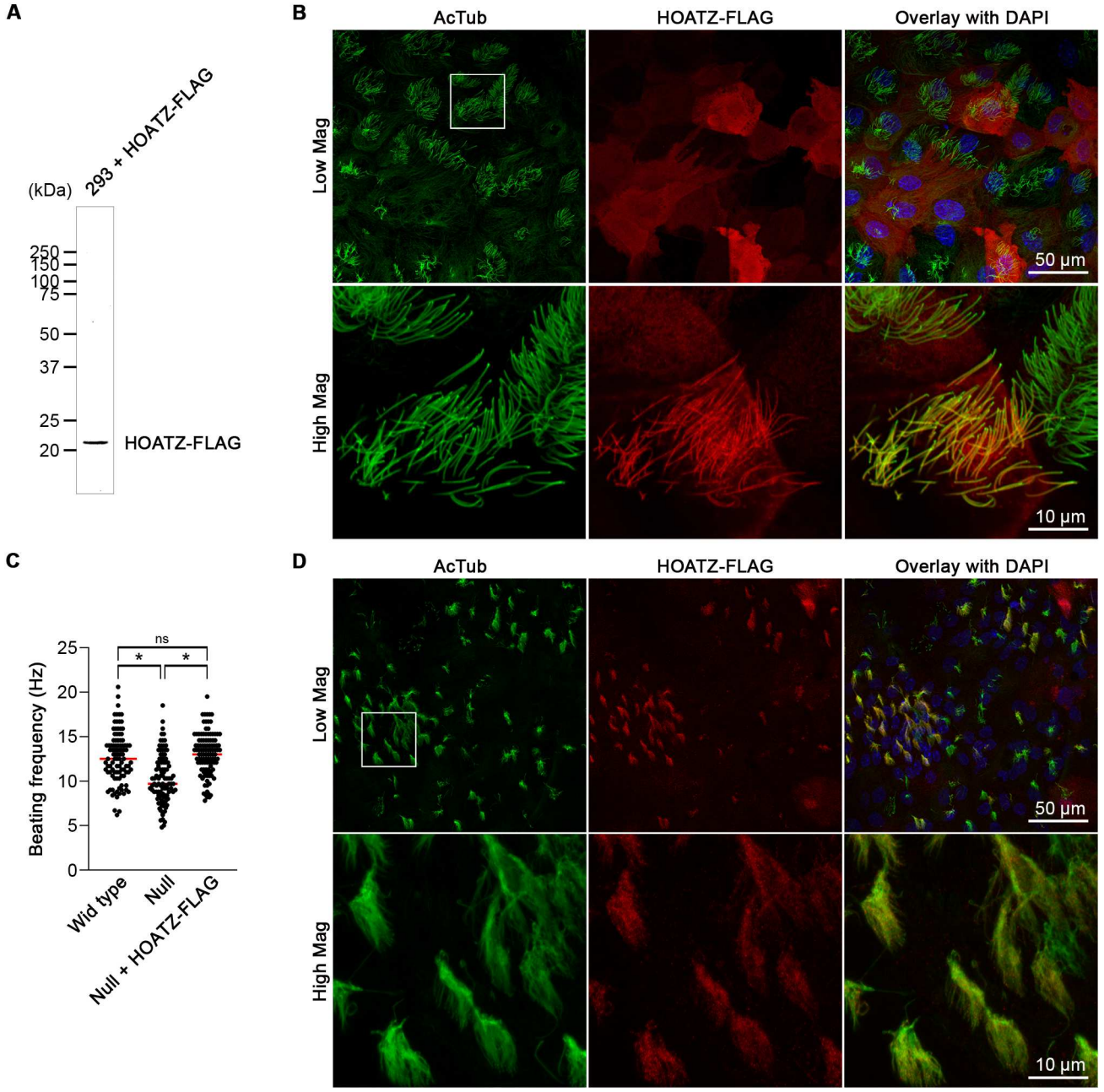
A
293 + HOATZ-FLAG
(kDa)
250
150
100
75
50
37
25
20
HOATZ-FLAG
B
AcTub
HOATZ-FLAG
Overlay with DAPI
Low Mag
High Mag
50 µm
10 µm
C
Beating frequency (Hz)
25
20
15
10
5
0
ns
*
*
Wid type
Null
Null + HOATZ-FLAG
D
AcTub
HOATZ-FLAG
Overlay with DAPI
Low Mag
High Mag
50 µm
10 µm

Supplemental Figure S1. Analysis of the subcellular localization of HOATZ-FLAG in cultured brain ependyma, Related to Figure 1. (**A**) Western blot analysis of HOATZ-FLAG expression. The proteins in a whole cell lysate of 293FT cells overexpressing HOATZ-FLAG were separated using a 5%–20% polyacrylamide gradient gel. The anti-FLAG antibody reacted with a protein that migrated at a position corresponding to 22 kDa (arrow). The positions and molecular masses (kDa) of the standards are indicated on the left. (**B**) Confocal fluorescence microscopy of cultured ependyma transduced with a lentiviral vector expressing HOATZ-FLAG under the control of the CMV promoter. The cells were analyzed for the expression of acetylated α-tubulin (green) and the FLAG epitope tag (red). Nuclei were detected using DAPI (blue). In the lower-magnification images, confocal sections were acquired from the base to the ciliary tip of the cells. In the higher-magnification images corresponding to the boxed area in the low magnification images, sections were limited to the apical space, including cilia. (**C**) Scatter plots with median lines showing the cilia beating frequencies of indicated cultured ependyma. High-speed video microscopy data were acquired in the same way as described for sperm flagellar beat frequency analysis. *$P < 0.0001$ between indicated groups ($n = 100$ cells for wild type, 103 for *Hoatz*$^{-/-}$, and 111 for *Hoatz*$^{-/-}$ + HOATZ-FLAG). (**D**) Confocal fluorescence microscopy of cultured *Hoatz*$^{-/-}$ ependyma transduced with a lentiviral vector expressing HOATZ-FLAG. The cells were analyzed for the expression of acetylated α-tubulin (green) and the FLAG epitope tag (red). Nuclei were detected using DAPI (blue).

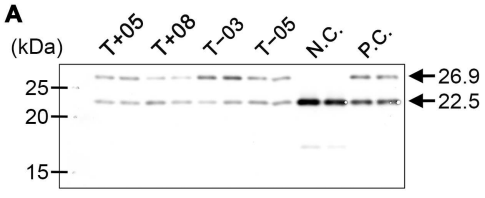

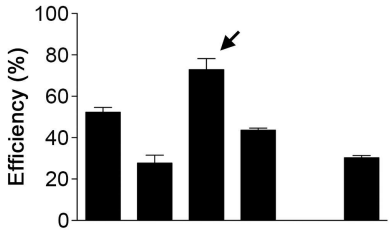

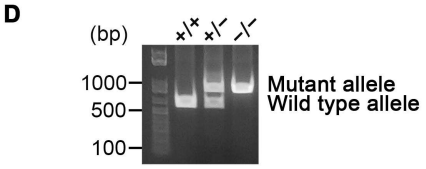

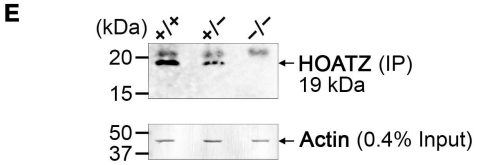

B

```
                                                   PAM   ▼        T-03
Wild type          tcaccATGGAAACGGGGCCCAGAGGCTGTCCTAGCGGCAGGAAGGAATCCCAGGAAATC..
                   -----MetGluThrGlyProArgGlyCysProSerGlyArgLysGluSerGlnGluIle..

Mut strain 1       tcaccATGGAAACGGGGCCCAGAGGCTGTCCTAGCGCAGGAAGGAATCCCAGGAAATCT..
c.31delG           -----MetGluThrGlyProArgGlyCysProSerAlaGlyArgAsnProArgLysSer..

Mut strain 2       tcaccATGGAAACGGGGCCCAGAGGCTGTCCTAGCCTAGCAGGAAGGAATCCCAGGAAA..
c.31delGinsCTA     -----MetGluThrGlyProArgGlyCysProSerLeuAlaGlyArgAsnProArgLys..
```

C

```
Wild type          caggcattccggtggtggcagttaccaacaggacggttctccggtaggggcgggacgccag
Mut strain 3       caggcattccggtggtggcag-------------------------------------
                                                                   PAM   ▼
Wild type          agctaaggaaagcgtcctgagtcaccATGGAAACGGGGCCCAGAGGCTGTCCTAGCGGCAG
Mut strain 3       ------------------------------------------------------------
                   T-03
Wild type          GAAGGAATCCCAGGAAATCTGCTCCCCTGGATTACTGGTGTTCACCGGCTGCTCTGAGCAG
Mut strain 3       -------------GAAATCTGCTCCCCTGGATTACTGGTGTTCACCGGCTGCTCTGAGCAG

Wild type          GATGCCAATTTGGCTAAGCAGTTTTGGCTCGGGGCGTCCATGTACCCCACTACCGAATCTC
Mut strain 3       GATGCCAATTTGGCTAAGCAGTTTTGGCTCGGGGCGTCCATGTACCCCACTACCGAATCTC

Wild type          AGCTCGTGCTGACCCGAGGCAG------------------------------------
Mut strain 3       AGCTCGTGCTGACCCGAGGCAGATTTACAAGTCAAACAGCCACAAGGAACTCTGAACAGAT

Wild type          ------------------------------------------------------------
Mut strain 3       TAGTGTGCACACTGTGACAGCTAACACAGACAACAGCCACGCAGGGCTGGTGCAAAGTACG

Wild type          ------------------------------------------------------------
Mut strain 3       TGCCTGGAAAACTCTATGTACAAAATAGTTCTCTGTAAACATGGTGAGGTGAATATTCCGA

Wild type          ------------------------------------------------------------
Mut strain 3       ACCCACTGAGAAGGATCTTCACTACAGGCAGAAATGTCACCCCCACACAGCACGAATGACA

Wild type          ------------------------------------------------------------
Mut strain 3       ACAGCTGAGGCCTCAGGCAGCCTGGAGACACAGTACTAAAAACGCAGGTGGCTGGGCTCAC

Wild type          ------------------------------------------------------------
Mut strain 3       CCTACAGGTCCTCTATAATTTTCTTATAAGTGAATGTGTGTCTGTGTGTGTGTATGTGTGT

Wild type          ------------------------------------CAGTCAGAGGCTACCGGTGGCGCG
Mut strain 3       GGTGTGTATACATAGGGATTTTTTTTTTGGCAGACAGCAGTCAGAGGCTACCGGTGGCGCG
```

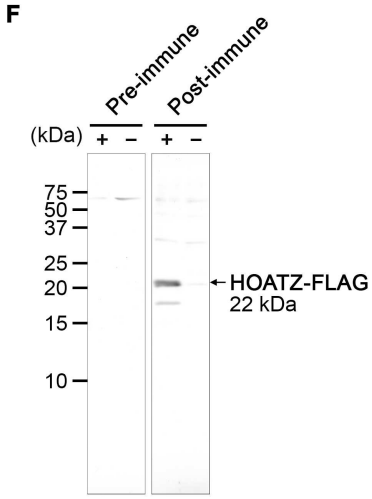

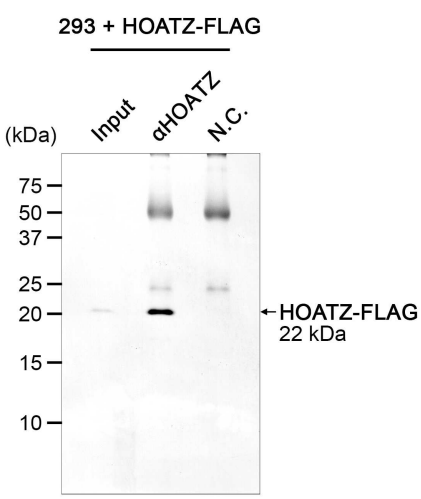

H

Genotype	Count	%
+/+	18	20
+/−	44	50
−/−	26	30

Supplemental Figure S2. Generation of *HOATZ*$^{-/-}$ mice using the CRISPR/Cas9 system, Related to Figure 2. (**A**) Quantitative analysis of the double-strand break efficiencies of pX330 clones targeting *Hoatz*. Top: Western blot analysis of 293T cells coexpressing one of the indicated pX330 clones (T+05, T+08, T−03, and T−05) and the pCAG-EGxxFP reporter construct containing the target region. The empty pX330 vector and the reporter construct served as negative controls, and the pX330 and pCAG-EGxxFP constructs for *Cetn1* (Mashiko et al., 2013) served as positive controls. The lower band (22.5 kDa) corresponds to the nonfluorescent fragment of EGFP encoded by the full-length pCAG-EGxxFP plasmid, whereas the 26.9-kDa band corresponds to full-length EGFP regenerated after the targeted double-strand break and subsequent repair processes. Bottom: The efficiencies of the pX330 clones were calculated according to the ratio of the intensities of each band, and values are expressed as the mean ± SEM (n = 2). (**B**) Nucleotide sequence analysis of *Hoatz* mutant strains #1 and #2. The position and direction of the T−03 guide RNA recognition sequence, the adjacent protospacer-adjacent motif (PAM), and the site of the targeted double-strand break are indicated on the wild-type reference sequence. (**C**) Nucleotide sequence analysis of *Hoatz* mutant strain #3. A relatively large deletion and insertion flanked by the CAG motif were introduced around the target site. (**D**) Genomic PCR analysis of strain #3. (**E**) Analysis of HOATZ expression in wild type, heterogeneous, and *Hoatz*$^{-/-}$ mouse testes at 10 weeks of age (strain #3). Whole testis extracts were immunoprecipitated using a rabbit anti-HOATZ polyclonal IgG, and the immunoprecipitates were analyzed using western blotting with the same anti-rabbit IgG. Rabbit TrueBlot (Rockland) was used as the secondary antibody to minimize the signal generated by IgG heavy and light chains. HOATZ (19 kDa) was undetectable in the *Hoatz*$^{-/-}$ mutant. A nonspecific band >20 kDa was present in all samples, which was a protein present in the testicular homogenate that bound to Protein G-Sepharose beads but was not detected when magnetic beads were used for immunoprecipitation. Pan-actin served as the loading control. (**F**) Specificity of the rabbit polyclonal anti-HOATZ antibody. Pre- and postimmune rabbit sera were used to probe a PVDF membrane containing proteins present in a whole cell lysate of 293T cells with (+) or without (−) expression of HOATZ-FLAG. The minor band (approximately 17 kDa) detected by the immune sera was a degradation product of recombinant HOATZ-FLAG. (**G**) Control immunoprecipitation experiment. HOATZ-FLAG overexpressed in 293-FT cells was immunoprecipitated using the rabbit anti-HOATZ antibody, resolved using a 15% polyacrylamide gel, and detected with the anti-FLAG antibody. Normal rabbit IgG served as a negative control. The faint bands present in the immunoprecipitates were the heavy and light chains of rabbit IgG. (**H**) Genotype distribution of offspring from heterozygous matings.

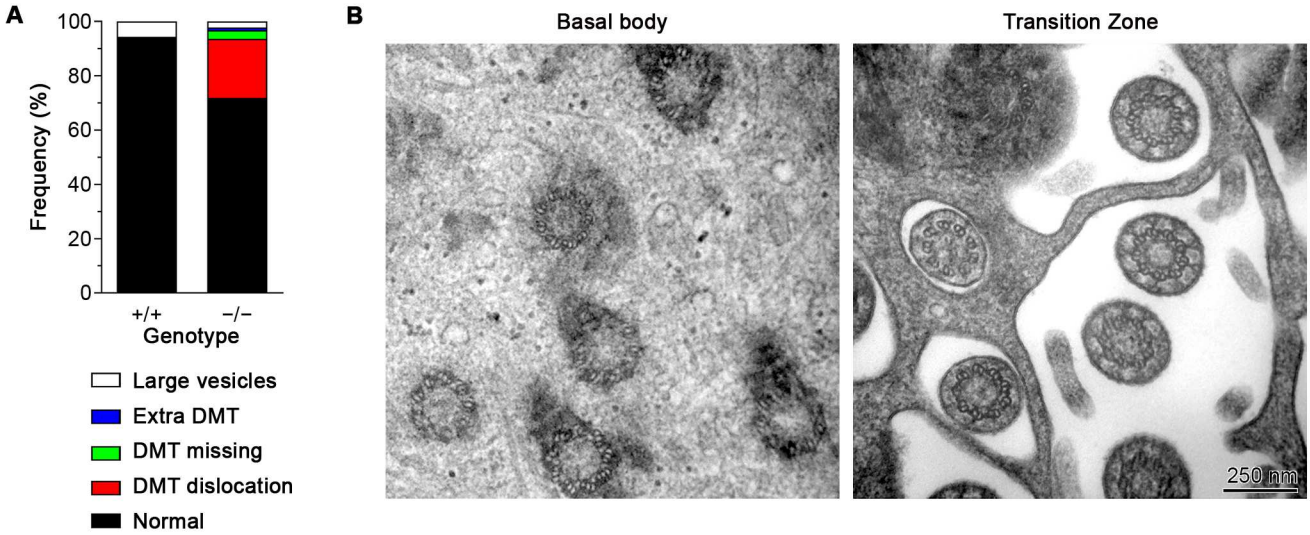
A
100
80
60
40
20
0
Frequency (%)
+/+
−/−
Genotype
Large vesicles
Extra DMT
DMT missing
DMT dislocation
Normal
B
Basal body
Transition Zone
250 nm

Supplemental Figure S3. Ultrastructural analysis of motile cilia in ependyma, Related to Figure 3. (**A**) Quantitative analysis of ciliary axoneme abnormalities. Horizontal sections of cilia of wild type (n = 387) and the *Hoatz*$^{-/-}$ mutant (n = 216) were inspected and classified into the indicated groups. (**B**) Representative TEM images of *Hoatz*$^{-/-}$ ependyma in the brain ventricle, showing apparently intact basal bodies and ciliary transition zones. Bar = 250 nm.

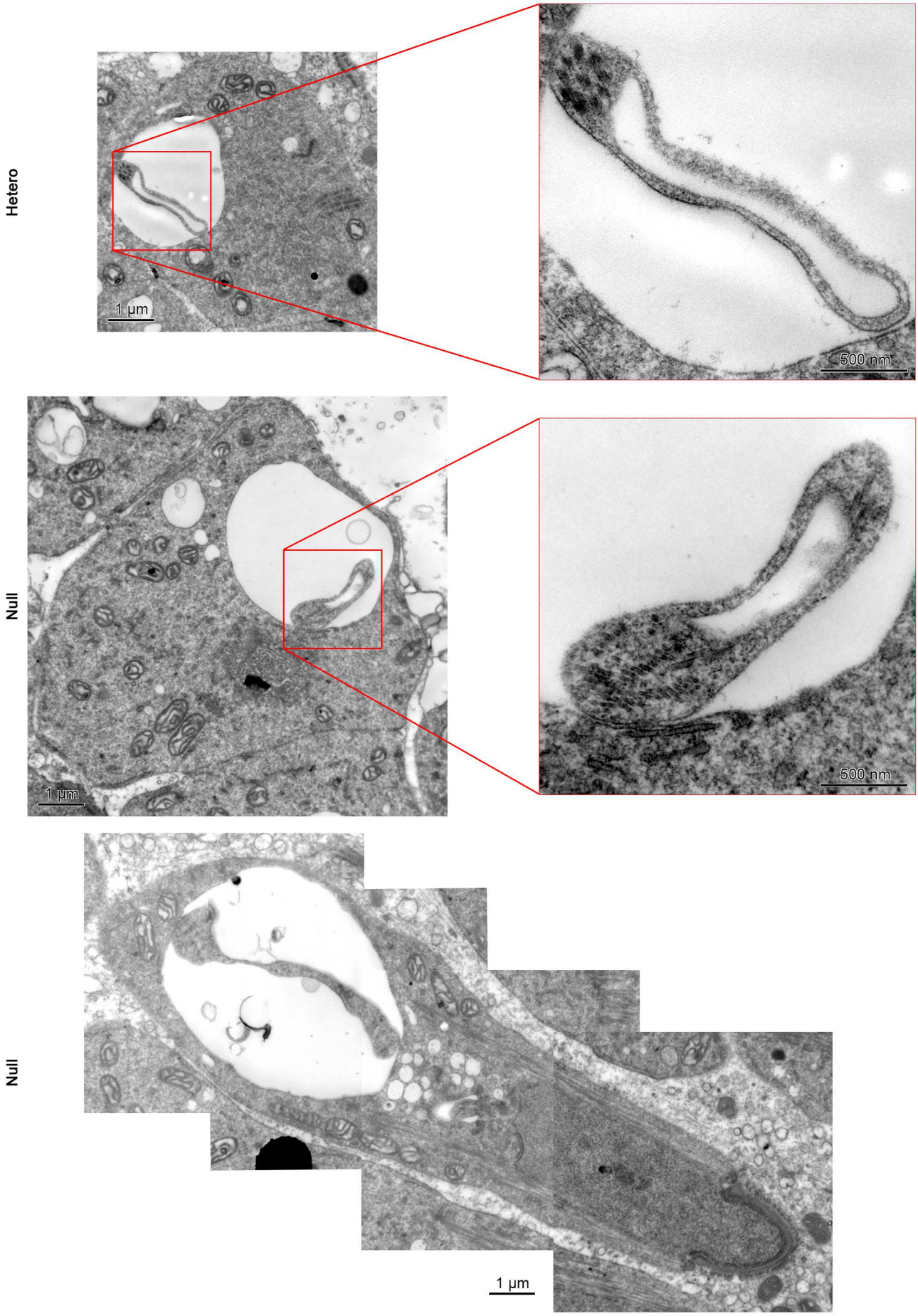
Hetero
1 µm
500 nm
Null
1 µm
500 nm
Null
1 µm

Supplemental Figure S4. Ultrastructural analysis of spermatids undergoing cytodifferentiation, Related to Figure 4. Representative TEM images of spermatids undergoing cytodifferentiation in the asymptomatic heterozygous and the *Hoatz*$^{-/-}$ mutants. In the *Hoatz*$^{-/-}$ mutant, a deformed flagellum contained a bundle of singlet microtubules (zoom). Abnormal intracellular vesicles were present in the cytoplasm.

A

Distal region

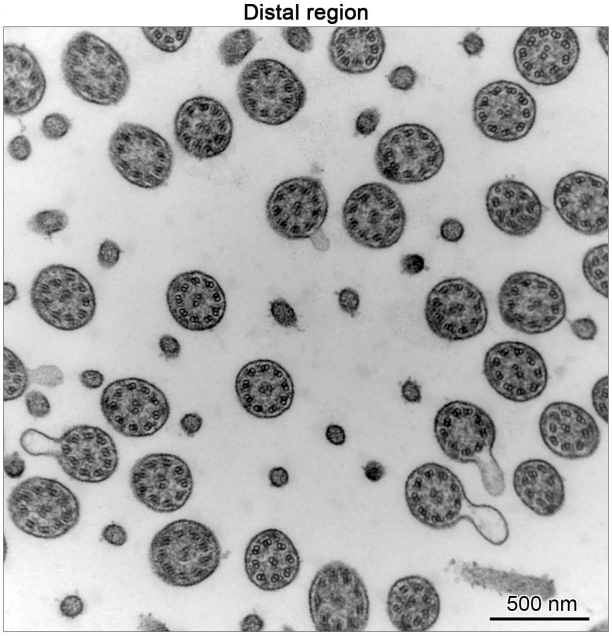

Distal region

Proximal region

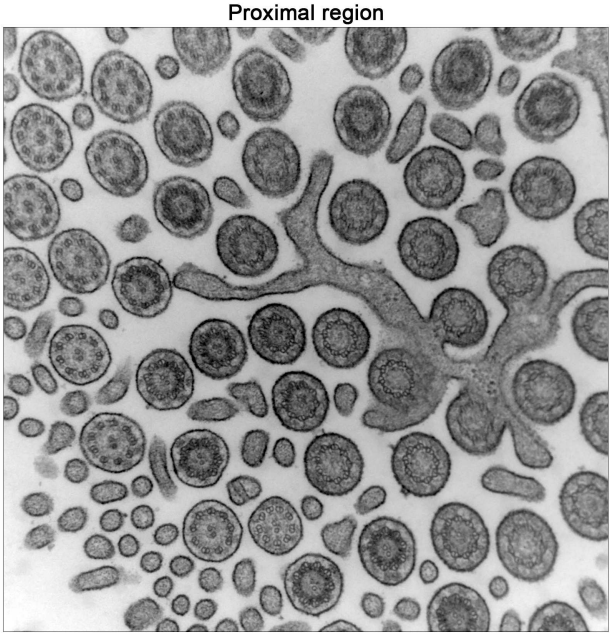

Basal body

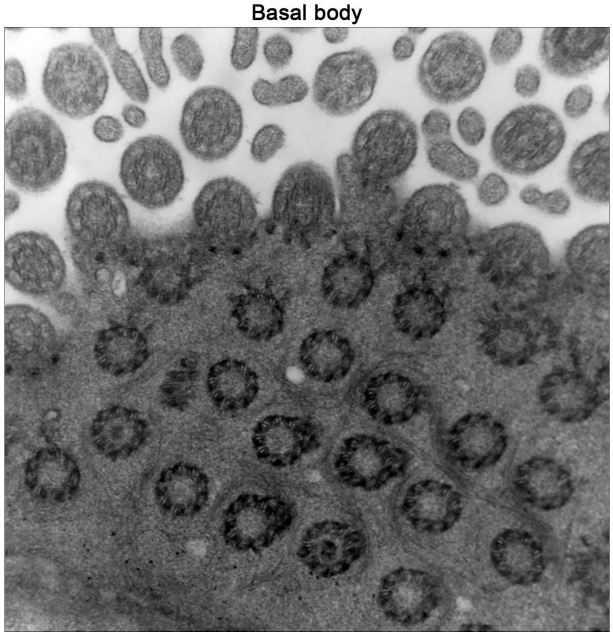

B

Wild type

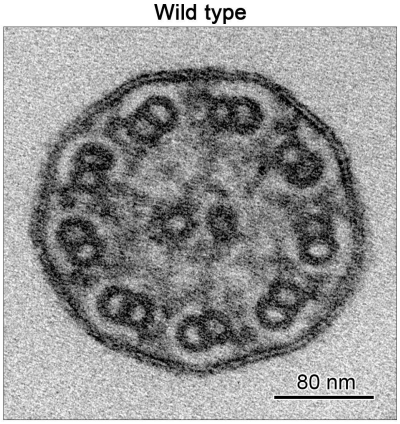

Null

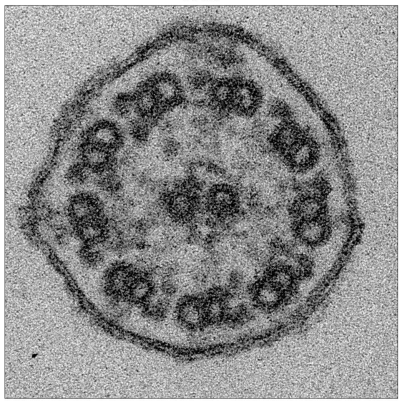

Microtubules	% (Null/WT)
Normal	95/95
Outer doublet defect	4/4
Central pair defect	0/0
Other defects	0/1

Dynein arms	% (Null/WT)
Normal	79/82
Outer arm defect	1/4
Inner arm defect	15/11
No arms	5/3

Supplemental Figure S5. Ultrastructural analysis of motile cilia in *Hoatz*$^{-/-}$ tracheal epithelia, Related to Figure 4. (**A**) Representative TEM images showing apparently intact structures. Bar = 500 nm. In the distal region of the cilia, there were several vesicle-containing swellings of axolemma, which represent ependymal cilia (Fig. 3C). (**B**) Representative higher magnification images of individual cross sections of cilia from wild type and *Hoatz*$^{-/-}$ trachea. The table summarizes the results of the quantitative analysis. For wild type control, 328 and 138 cilia were analyzed to score the structural integrity of 9+2 microtubules and the dynein arms, respectively. For *Hoatz*$^{-/-}$ mutant, 322 and 162 cilia were analyzed likewise. A detailed description of the analysis is provided in the Method section (Shoemark et al., 2012, 2020).

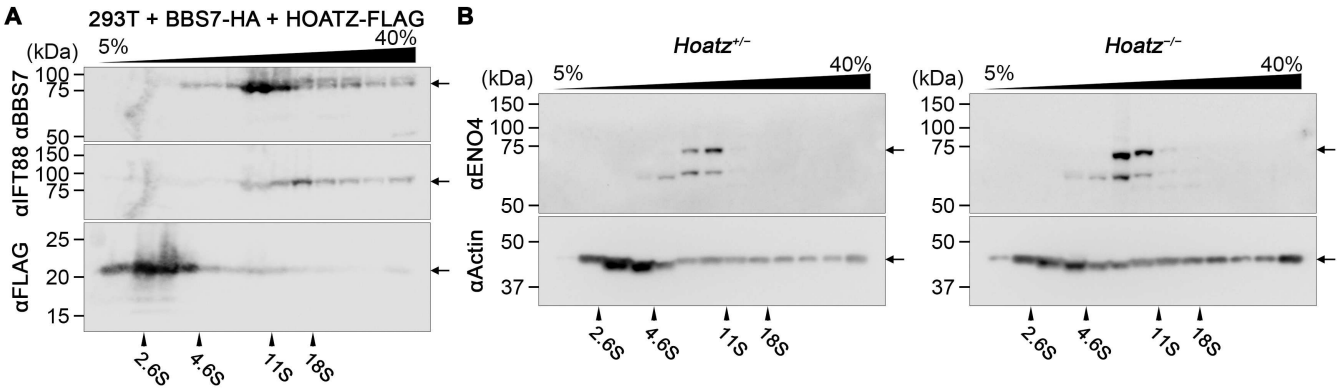
A
293T + BBS7-HA + HOATZ-FLAG
(kDa)
5%
40%
αBBS7
αIFT88
αFLAG
100
75
50
150
100
75
25
20
15
2.6S
4.6S
11S
18S
B
Hoatz+/−
Hoatz−/−
(kDa)
5%
40%
αENO4
αActin
150
100
75
50
50
37
2.6S
4.6S
11S
18S

Supplemental Figure S6. Abnormal accumulation of ENO4 in *Hoatz*$^{-/-}$ ependyma, Related to Figures 5 and 6. (**A**) Sucrose density gradient analysis of 293T cells overexpressing BBS7-HA and HOATZ-FLAG. Western blot analysis of the distributions of BBS7, IFT88 and recombinant HOATZ. (**B**) Western blot analysis of ENO4 levels of the asymptomatic heterozygous and *Hoatz*$^{-/-}$ mouse ependyma.

Transparent Methods

Mice and cell culture

The Institutional Animal Care and Use Committee at the University of Yamanashi approved the experiments using mice (Approval number: 29-43). C57BL/6J mice were from Charles River Laboratories Japan (Yokohama, Japan). Primary cultures of mouse ependyma were prepared from mechanically dissociated neonatal mouse cerebral hemispheres seeded on Matrigel-coated culture dishes (Narita et al., 2012). The cells were grown in Neurobasal-A medium containing B27 supplement (Thermo Fisher Scientific), while contaminating neurons were washed out by applying a stream of culture medium before changing the medium. Lenti-X 293T cells (Takara Bio, Shiga, Japan) and the 293FT cell line (Thermo Fisher Scientific, Waltham, MA) were cultured following the sources' instructions.

Molecular cloning, mammalian gene expression, and RNA in situ hybridization

The *Hoatz* cDNA was amplified from a cDNA library of cultured mouse ependyma using KOD Plus Neo DNA polymerase (Toyobo, Osaka, Japan) and the custom oligonucleotide primers (Thermo Fisher Scientific) with restriction sites indicated as follows: Hoatz BamHI Fwd (5′-ggatccATGGAAACGGGGCCCAGAGG-3′); Hoatz XhoI Rev (5′-ctcgagTTCCAAGGCTTTGACTTCTTCTTGGTCC-3′). The annealing temperature was 65 °C. The PCR product was cloned into the pGEM-T Easy vector (Promega, Madison, WI), and the sequence was confirmed. To express HOATZ-FLAG in mammalian cells, the *Hoatz* cDNA was cleaved from the cloning vector and ligated to the BamHI-XhoI sites of pCMV-Tag 4A (Agilent Technologies, Santa Clara, CA). For lentiviral expression of HOATZ-FLAG, the coding region of the pCMV-Tag 4A clone was amplified with KOD Plus Neo using the above BamHI Fwd and universal T7 promoter primers and then ligated to the Eco47III site of CSII-CMV-MCS-IRES2-Bsd (provided by Dr. Hiroyuki Miyoshi [RIKEN BioResource Center] along with the packaging plasmids pCAG-HIVgp and pCMV-VSV-G-RSV-Rev). For knockdown experiments, five pLKO1.puro lentiviral shRNA clones targeting *Hoatz* mRNA (TRCN0000190637, TRCN0000190708, TRCN0000201642, TRCN0000201968, TRCN0000201969) and a mock shRNA control (RHS4080) were obtained from Dharmacon (Lafayette, CO, USA). These lentiviral constructs were packaged into the VSV-G pseudotyped lentivirus and transduced into cultured mouse ependyma (Shamoto et al., 2018).

RNA *in situ* hybridization: *Hoatz*-specific digoxigenin (DIG)-labeled sense and antisense RNA probes were synthesized using a DIG RNA labeling kit (Roche Applied Science, Penzberg, Germany) and the linearized pGEM-T construct described above and then purified using an RNeasy Mini kit (Qiagen, Venlo, Netherlands). RNA *in situ* hybridization was performed as described (Kawaguchi et al., 2008).

Reverse transcription and polymerase chain reaction

Total RNA extraction, reverse transcription, and polymerase chain reaction were performed using Trizol reagent (Thermo Fisher Scientific), High Capacity cDNA reverse transcription kits (Thermo Fisher Scientific) and KOD Plus Neo DNA polymerase, respectively (Shamoto et al., 2018), following manufacture's instructions.

The same primer pair described above was used for semiquantitative analysis of *Hoatz* mRNA levels. The *Gapdh* primers were as follows: Gapdh Fwd, 5′-AACTTTGGCATTGTGGAAGG-3′; Gapdh Rev, 5′-ACACATTGGGGGTAGGAACA-3′. The annealing temperature for *Gapdh* was 60 °C. The concentrations of template cDNA samples were adjusted so that the amplicon of *Gapdh* at 25 cycles yielded similar band intensities on the agarose gel, determined using ImageJ (Schneider et al., 2012). PCR was performed for 27 cycles.

Real-time PCR analysis of *Eno4* mRNA: The Thunderbird SYBR qPCR mix (Toyobo) was used, and the amplicons were analyzed using a StepOnePlus Real-time PCR System (Thermo Fisher Scientific) following the manufacturer's instructions. The primer sequences were as follows: Eno4 Fwd, 5′-GGGTGAACGGATGACCAAATA-3′; Eno4 Rev, 5′-CCCCTCTGGATGAGTTCTTCCT-3′; B2m Fwd, 5′-CACTGACCGGCCTGTATGC-3′; B2m Rev, 5′-GGTGGCGTGAGTATACTTGAATTTG-3′. The annealing temperature was 59 °C.

Antibodies

Mouse anti-acetylated α-tubulin (6-11B-1) and rabbit anti-ENO4 (HPA037938) were procured from Sigma-Aldrich (St. Louis, MO). Rabbit anti-ARL13B (17711-1-AP) were obtained from Proteintech (Rosemont, IL). The anti-IFT88 antibody was provided by Prof. Gregory J Pazour, University of Massachusetts Medical School (Pazour et al., 2002). Mouse anti-pan actin (MS-1295-P0), rabbit anti-GFP (A-6455), and Alexa Fluor-conjugated secondary antibodies were from Thermo Fisher Scientific (Waltham, MA). Rabbit anti-DYKDDDDK as well as horseradish peroxidase-conjugated secondary antibodies were from Cell Signaling Technologies (Danvers, MA). Rabbit TrueBlot anti-rabbit IgG HRP (18-8816-33) was from Rockland Immunochemicals (Limerick, PA).

To generate rabbit polyclonal antibodies against HOATZ, the full-length mouse *Hoatz* cDNA, fused to a poly-histidine tag at its 3′ end and flanked by BamHI and XhoI restriction sites, was PCR-amplified and ligated to pGEX6P-1 (GE Healthcare Japan, Tokyo, Japan). The resulting construct was used to transform *Escherichia coli* strain BL21(DE3) (BioDynamics Laboratory, Tokyo, Japan). Recombinant GST-HOATZ-poly(His) was expressed, purified using His60 Ni Gravity Columns (Takara Bio, Shiga, Japan) in the presence of 6M guanidine hydrochloride, precipitated with 5% (v/v) trichloroacetic acid, and rinsed with acetone. The protein pellet (5.6 mg from 500 ml bacterial culture) was dissolved in 200 µl of the denaturing buffer and used to immunize rabbits at Genenet (Fukuoka, Japan). The IgG was purified using Protein G Sepharose 4 Fast Flow (GE Healthcare Japan). Affinity purification of anti-HOATZ antibodies was performed using a strip of PVDF membrane containing purified GST-HOATZ-poly(His) that was transferred from SDS-PAGE gel (Olmsted, 1981). The membrane was incubated with anti-HOATZ IgG diluted in TBST containing 10% bovine serum albumin and 2% sodium azide, and the bound antibodies were eluted with 0.1 M glycine buffer, pH 2.8. The eluate was neutralized immediately by 1M Tris-HCl, pH 8.0, concentrated with Vivaspin 500 column (Sartorius, Göttingen, Germany), supplemented with glycerol to a final concentration of 50% and stored at –30 °C.

Generation of Hoatz$^{-/-}$ mice using the CRISPR/Cas system

Hoatz was mutated through pronuclear injection of pX330 (Addgene plasmid #42230) according to Cong et al (Cong et al., 2013) and Mashiko et al (Mashiko et al., 2013), and in detail elaborated here. First, guide RNAs targeting exon 1 of mouse *Hoatz* (chromosome 9) were designed using the CRISPRdirect server program (Naito et al., 2014), and those targeting sequences immediately downstream of the first methionine codon with minimum off-targeting scores were selected. The following four oligonucleotide pairs were annealed and ligated into the BbsI site of pX330, to generate the clones designated T+05, T+08, T−03, and T−05: T+05 Fwd, 5′-caccAGGCTGTCCTAGCGGCAGGA-3′; T+05 Rev, 5′-aaacTCCTGCCGCTAGGACAGCCT-3′; T+08 Fwd, 5′-caccAATCTGCTCCCCTGGATTAC-3′; T+08 Rev, 5′-aaacGTAATCCAGGGGAGCAGATT-3′; T−03 Fwd, 5′-caccTGGGATTCCTTCCTGCCGCT-3′; T−03 Rev, 5′-aaacAGCGGCAGGAAGGAATCCCA-3′; T−05 Fwd, 5′-caccATCCAGGGGAGCAGATTTCC-3′; T−05 Rev, 5′-aaacGGAAATCTGCTCCCCTGGAT-3′. A 600-bp fragment of the mouse genome containing the target sites were cloned into the EcoRI-BamHI sites of pCAG EGxxFP (Addgene plasmid #50716) to generate the reporter plasmid for the *in vitro* double-strand break assay. The primer pairs were as follows: Fwd, 5′-gaattcAGATCTACGGAAGAAGAAACACAGGC-3′; Rev, 5′-ggatccGTGAGCCACCATGTGGTTGC-3′. The resulting pCAG EGxxFP and one of the pX330 constructs were used to cotransfect HEK293T cells using lipofection, and the efficiencies of the targeted double-strand break were determined by measuring green fluorescence using fluorescence microscopy and western blotting. Constructs of *Cetn1* (provided by Dr. Masahito Ikawa, Osaka University) (Mashiko et al., 2013) served as a control. Clone T−03, showing the highest double-strand break efficacy (supplemental Fig S1), was microinjected into BDF1×B6 zygotes at Advanced Biotechnology Center, University of Yamanashi. The resulting F0 animals were backcrossed with C57BL/6J, and the F1 progeny were genotyped to confirm germline transmission. The PCR primers used for genotyping of strain #3 were as follows: *Hoatz* exon1 Fwd, 5′-TCCACCGGTACTTCTCGGCCC-3′; *Hoatz* exon 1 Rev, 5′-CGCGCCACCGGTAGCCTCTG-3′. The annealing temperature was 65 °C.

Epididymal sperm were counted as previously described (Wang, 2003). Briefly, the cauda epididymis was isolated in PBS, weighed, and then cut into fine pieces in 1 ml of PBS using ophthalmic scissors and a stereomicroscope. After incubation at room temperature for 1 h, the sperm released into PBS were passed through a 100-μm mesh cell strainer to remove tissue debris, diluted as required, heat-inactivated, and counted using a hemocytometer.

Live imaging analyses

Analysis of the motility of ependymal cilia: FluoSpheres polystyrene microspheres (1.0-μm diameter, yellow-green fluorescence) (Thermo Fisher Scientific, Waltham, MA) were suspended in DMEM at approximately 1×10^8 beads/ml and added to a 35-mm glass-bottom culture dish (Nippon Genetics, Tokyo, Japan) containing a confluent primary culture of ependyma. After incubation for 3 min at room temperature, the cells were rinsed three times to remove excess beads and then observed using a fluorescence microscope. We previously found that the tips of the beating cilia occasionally adhered to the fluorescent microbeads. Thus, the beating of such “labeled”

cilia were traced using fluorescence microscopy (Katoh et al., 2018), and in detail elaborated here. At visible wavelengths, the adherent beads that beat at high frequencies appeared as short lines of fluorescence and were therefore distinguished from the other floating or nonbeating beads. We aimed to analyze the beating amplitude of motile cilia in cell culture using the "analyze particles" function of ImageJ. The images of the fluorescent microbeads on an ependymal monolayer were acquired at room temperature using an Olympus IX71 microscope equipped with UPlanSApo 10×/0.40 objective and DP72-cooled CCD color camera equipped with DP2-BSW software. The exposure time was 50-100 ms, and the image resolution was 1.54 pixels/µm.

The images capturing the traces of numerous beating beads were analyzed using ImageJ as follows: The acquired color images were first converted to 8-bit grayscale, and the background associated with a rolling ball radius of 20 was subtracted. A common threshold level that would best separate the bead tracings and background was then set for particle analysis. Then open "set measurement" dialog and select "shape descriptors" and "fit ellipse" options to measure the lengths of the major and minor axes of an ellipse fitting a selected region of interest and used to calculate the aspect ratio (major axis divided by minor axis). Using the same dialog, "Integrated density" was selected. Upon executing the "analyze particles" command, only 50–200 pixel^2 particles, circularities ranging from 0–0.80, were selected in the dialog window to exclude overlapped, aggregated, or static beads. Further, select "outlines" from the "show" option in the same dialog was used to determine if the regions of interest were properly selected and subsequently analyzed.

When a trace of a beating bead is analyzed, the values of the major and minor axes should correspond to the apparent beating amplitude and apparent bead diameter, respectively (Fig. 3B). The actual bead diameter was uniform and constant, although the apparent bead diameter measured using fluorescence microscopy varied depending on the degree of defocus. To minimize the influence of defocus on the measurement of the beating amplitude, the apparent beating amplitude was divided by the apparent bead diameter to calculate the normalized beating amplitude, which represents the aspect ratio of the normalized beating amplitude. Finally, a cumulative frequency distribution plot of the normalized beating amplitude was generated using GraphPad Prism software.

Analysis of the motility of sperm flagella: A pair of cauda epididyma was isolated, cut into small pieces using microscissors in 1-ml Leibovitz L-15 medium, and incubated at room temperature for 1 h. The samples were then filtered through 100-µm Falcon Cell Strainers (Corning, Corning, NY) to remove tissue debris, diluted (typically 1:2000), transferred to a 35 mm glass-bottom culture dish, and observed using an Olympus IX70 inverted microscope equipped with a 100-W mercury lamp, differential interference contrast optics, a UPlanSApo 20×/0.75 objective, and an Allied GE680 CCD camera. The images were recorded at 175 frames/s and analyzed using TI Workbench software (Fukatsu et al., 2004). The (number of frames per second)/(average number of frames of a single beat) (CBF) was calculated (Chilvers and O'Callaghan, 2000). To characterize flagellar beating patterns, we superimposed 10 representative frames acquired during one beating cycle.

Electron microscopy

Samples for SEM and TEM were fixed in half Karnovsky fixative (0.1 M cacodylate buffer, pH 7.4, 2 % paraformaldehyde, 2.5% glutaraldehyde) containing 0.2% tannic acid (Fujifilm Wako Pure Chemical, Osaka, Japan), then washed with 0.1 M cacodylate buffer containing 10% sucrose, post-fixed with 1% osmium tetroxide for 1 h on ice, and dehydrated with graded concentrations of ethanol (Narita et al., 2010, 2012; Nonami et al., 2013). For SEM analysis of sperm, samples suspended in ethanol were dried on a glass coverslip glued on a metal specimen mount, and sputter-coated with platinum. For TEM analysis, samples were further dehydrated with propylene oxide and embedded in epoxy resin.

Transverse sections of cilia from wild type and *Hoatz*$^{-/-}$ mouse trachea were analyzed as described elsewhere (Shoemark et al., 2012, 2020) to assess the ultrastructural integrity in a quantitative manner. Briefly, ultrathin sections of epon-embedded tissue specimens were stained with uranyl acetate and lead citrate and observed under JEM-2100F field emission electron microscope (JEOL, Tokyo, Japan) at an acceleration voltage of 120 kV. Digital images were acquired at 30,000–40,000 × magnifications using a bottom mount TemCam-F216 CMOS camera (TVIPS, Gauting, Germany). Then the 9+2 microtubules of >300 cilia and the dynein arms of >100 cilia were assessed to calculate the scores for each specimen, based on a definition of the hallmark diagnostic defects (class 1 defects) described in the international consensus guideline for reporting transmission electron microscopy results in the diagnosis of primary ciliary dyskinesia (Shoemark et al., 2020).

Sucrose density gradient centrifugation, immunoprecipitation, and shotgun proteomics

For sucrose density gradient fractionation, one pair of testes was isolated from an adult mouse and placed in ice-cold PBS. After measuring the wet weight (mg), the tunica albuginea was removed. The tissue sample was then transferred into a 2-ml glass/Teflon tissue grinder containing 1 ml of ice-cold LAP150 buffer (50 mM HEPES, pH 7.4, 150 mM KCl, 1 mM EGTA, 1 mM $MgCl_2$) containing 0.3% (v/v) Igepal CA-630, 1 mM dithiothreitol, and protease inhibitor cocktail (#P2714, Sigma-Aldrich) and was then homogenized (Nachury et al., 2007). After centrifugation at 10,000 × g for 10 min at 4 °C to remove debris, the supernatant was loaded onto a 9-ml 5%–40% linear sucrose gradient in LAP150 buffer containing 0.3% Igepal CA-630 and then centrifuged at 4 °C in a CP80WX Himac Utracentrifuge (Hitachi Koki, Tokyo, Japan) equipped with a Beckman SW41 rotor. The cumulative centrifugal effect ($\omega^2 t$) was set to 8.3×10^{11} rad^2/s. The sedimentation standards bovine pancreas chymotrypsinogen A (2.6S), bovine serum albumin (4.6S), bovine liver catalase (11.3S), and horse spleen apoferritin (17.6S) were from Sigma-Aldrich. After centrifugation, 13 fractions (approximately 770 µl each) were collected from the top of the tube using a DGF-U fractionator (Hitachi Koki, Tokyo, Japan).

For immunodetection, the proteins in the density gradient fractions were precipitated with 5% (v/v) trichloroacetic acid, rinsed twice with cold methanol, dried briefly, and dissolved in 4× SDS sample buffer. To adjust the loading between different animals, the sample buffer was added to each fraction tube at 50 µl per 60 mg of tissue weight measured before homogenization.

For immunoprecipitation and shotgun proteomics, the fractions #3–#8 containing HOATZ were pooled, and an aliquot (approximately 1.5 ml) was incubated for 3 h at 4 °C with 50 µl of Dynabeads Protein G (Veritas, Tokyo, Japan) that was crosslinked to affinity-purified anti-HOATZ antibodies. The beads were then washed three times, 10 min each, with LAP150 buffer containing 0.3% Igepal CA-630; rinsed twice briefly with the same buffer without detergent; and incubated for 2 min in 30 µl of 0.1 M glycine buffer, pH 2.8, to elute the bound proteins. The eluate was transferred to a new tube and neutralized with 3 µl of 1 M Tris-HCl, pH 8.0. These steps were repeated twice, with the final incubation overnight instead of 3 h. The eluates were pooled, digested with trypsin and subjected to shotgun proteomic analyses using Dina-2A nanoflow LC system (KYA Technologies, Tokyo, Japan) coupled with LTQ-Orbitrap Velos mass spectrometer (Thermo Fisher Scientific, Bremen, Germany) (Contu et al., 2017). The samples were injected into a 75 µm reversed-phase C18 column at a flow rate of 10 µl/min, and eluted with a linear gradient of solvent A (2% acetonitrile and 0.1% formic acid in H_2O) to solvent B (40% acetonitrile and 0.1% formic acid in H_2O) at 300 nl/min. The separated peptides were then sequentially sprayed from a nanoelectrospray ion source (KYA Technologies) and analyzed by collision-induced dissociation. The analyses were operated in data-dependent mode, switching automatically between MS and tandem mass spectrometry (MS/MS) acquisition. For collision-induced dissociation analyses, full-scan MS spectra (from 380 to 2000 *m/z*) were acquired in the orbitrap with resolution of 100,000 at 400 *m/z* after ion count accumulation to the target value of 1,000,000. The 20 most intense ions at a threshold above 2000 were fragmented in the linear ion trap with normalized collision energy of 35% for an activation time of 10 ms. The orbitrap analyzer was operated with the 'lock mass' option to perform shotgun detection with high accuracy. Protein identification was conducted by searching MS and MS/MS data against the RefSeq (National Center for Biotechnology Information) mouse protein database (29,579 protein sequences as of 4 February, 2013) by Mascot version 2.5.1 (Matrix Science). Methionine oxidation, protein N-terminal acetylation, and pyroglutamination for N-terminal glutamine, were set as variable modifications. A maximum of two missed cleavages was allowed in our database search, while the mass tolerance was set to 3 ppm for peptide masses and 0.8 Da for MS/MS peaks, respectively. In the process of peptide identification, we conducted decoy database searching by Mascot and applied a filter to satisfy a false positive rate <1%.

Western blotting and immunohistochemistry

Western blotting and immunohistochemistry were performed following standard protocols (Narita et al., 2015). In brief, for western blotting, proteins resolved by SDS-PAGE were transferred onto PVDF membrane using a wet transfer system, at 5V overnight at room temperature. The resulting blots were blocked with 10% skim milk in TBST, incubated with the primary antibodies overnight at 4 °C, washed three times with TBST, incubated with HRP-conjugated secondary antibodies for 1 hour at room temperature, washed three times again, and incubated with Chemi-Lumi One Super substrate (Nakalai Tesque, Kyoto, Japan) in ImageQuant LAS-4000 lumino analyzer (GE Healthcare Japan) for detection. For immunohistochemistry, sections of 4% paraformaldehyde-fixed tissues on glass slides were autoclaved in 20 mM Tris-HCl, pH 9.0, containing 10% sucrose for heat-induced

epitope retrieval, and blocked with 10% skim milk in TBST. Then the samples were incubated with the primary antibodies in the blocking buffer overnight at 4 °C, washed three times with TBST, incubated with the Alexa-conjugated secondary antibodies for 2 hours at RT, washed again, and sealed with an antifade mounting medium containing DAPI. For the immunohistochemical analysis of testis sections for ENO4 expression, the tissue was cut in half by razor blades, fixed with 4% paraformaldehyde in PBS by immersion, embedded in OCT compound, and cut into 5 μm thick slices onto a glass slide. The sections were dried, boiled for 5 min in 10 mM citrate buffer, pH 6.0, for epitope retrieval, washed three times in PBS containing 0.1% Triton X-100, and blocked with 20% goat serum in PBST (Dong et al., 2014).

For western blotting, primary antibodies were diluted 1:500, except anti-AcTub (1:1000). Antibody dilutions used for immunohistochemistry were as follows: acetylated α-tubulin (1:1,000), ARL13B (1:500), and ENO4 (1:50).

Statistical analysis

The significance of differences between two groups were evaluated using two-tailed *t* tests. Differences between multiple groups were analyzed using the nonparametric Kruskal–Wallis test that does not assume a Gaussian distribution, followed by Dunn's multiple comparison post hoc test. $P < 0.05$ indicates a significant difference.